Supporting data

for

Synthesis of the High Value Fragrances (Dihydrolinalool and Tetrahydrolinalool) using Combinations of Biobased Mint Biochar/ Activated charcoal incorporated Ni-Pd Catalysts

Kamlesh Yadav, Prasanta K Rout, Shubham Srivastava and Chandan S Chanotiya

Scheme

Plant Materials

Figure S1 Field view of the full-grown plant of *Ocimum basilicum* variety CIM- Shishir (A) and close up view (B)

Experimental

Figure S2 (A) XRD pattern, (B) FT-IR spectra, and (C) TGA curve of Ni-Pd/BC catalyst.

Figure S3 (A) SEM image of BC, (B) SEM image of 1%Ni-4%Pd/BC, (C-D) TEM image of 1%Ni-4%Pd/BC, and (E) EDS spectra of 1%Ni-4%Pd/BC.

Figure S4 (A-D) XPS analysis of catalyst (1%Ni-4%Pd/BC), (A) XPS survey, (B) C1s binding state, (C) Ni 2p binding state (D) Pd 3d binding state

Figure S5 (A) XRD pattern, (B) FT-IR spectra, and (C) TGA curve of Ni-Pd/AC catalyst.

Figure S6 N_2 isotherm (adsorption-desorption) of base materials and catalysts at 77K

Figure S7 Reusability investigation of composite 1% Ni-Pd 4%P/BC & 2%Ni-8%Pd/AC

Table S1: Characterization of Surface area and porosity

Table S2 Catalytic performance comparison of various catalysts for the hydrogenation of linalool to dihydrolinalool (DHL)

Table S3 Chemical compositions of pure and modified essential oils of *O. basilicum* var. CIM-Shishir

Table S4 Catalytic performance comparison of various catalysts for the hydrogenation of linalool to tetrahydrolinalool (THL)

GC-FID and GC-MS analysis

Figure S8.1 Mass spectrum of reaction substrate (I)

Figure S8.2 Mass spectrum of reaction product (IV)

Figure S8.3 Mass spectrum of reaction product (II)

Figure S8.4 Mass spectrum of reaction product (III)

Figure S8.5 Total ion chromatogram of essential oil extracted from aerial parts of *Ocimum* basilicum variety CIM-Shishir essential oil

Figure S8.6 Total ion chromatogram of modified essential oil with 1%Ni-4%Pd/BC and 2%Ni-8%Pd/AC

NMR analysis

Figure S9.1 ^{1}H-NMR (500 MHz, $CDCl_3$) spectrum of reaction substrate (I)

Figure S9.2 ^{13}C-NMR (125 MHz, $CDCl_3$) spectrum of reaction substrate (I)

Figure S9.3 DEPT 135° (125 MHz, $CDCl_3$) spectrum of reaction substrate (I)

Figure S9.4 DEPT 90° (125 MHz, $CDCl_3$) spectrum of reaction substrate (I)

Figure S9.5 DEPT 45° (125 MHz, $CDCl_3$) spectrum of reaction substrate (I)
Figure S9.6 1 H-^{1}H COSY ($CDCl_3$, 500 MHz) spectrum of reaction substrate (I)
Figure S9.7 ^{1}H-^{13}C HSQC (125 MHz, $CDCl_3$) spectrum of reaction substrate (I)
Figure S9.8 ^{1}H-^{13}C HMBC (125 MHz, $CDCl_3$) spectrum of reaction substrate (I)

Figure S10.1 ^{1}H-NMR (500 MHz, $CDCl_3$) spectrum of reaction product (II)
Figure S10.2 ^{13}C-NMR (125 MHz, $CDCl_3$) spectrum of reaction product (II)
Figure S10.3 DEPT 135° (125 MHz, $CDCl_3$) spectrum of reaction product (II)
Figure S10.4 DEPT 90° (125 MHz, $CDCl_3$) spectrum of reaction product (II)
Figure S10.5 DEPT 45° (125 MHz, $CDCl_3$) spectrum of reaction product (II)
Figure S10.6 **^{1}**H-^{1}H COSY ($CDCl_3$, 500 MHz) spectrum of reaction product (II)
Figure S10.7^{1}H-^{13}C HSQC (125 MHz, $CDCl_3$) spectrum of reaction product (II)
Figure S10.8^{1}H-^{13}C HMBC (125 MHz, $CDCl_3$) spectrum of reaction product (II)

Figure S11.1 ^{1}H-NMR (500 MHz, $CDCl_3$) spectrum of reaction product (III)
Figure S11.2 ^{13}C-NMR (125 MHz, $CDCl_3$) spectrum of reaction product (III)
Figure S11.3 DEPT 135° (125 MHz, $CDCl_3$) spectrum of reaction product (III)
Figure S11.4 DEPT 90° (125 MHz, $CDCl_3$) spectrum of reaction product (III)
Figure S11.5 DEPT 45° (125 MHz, $CDCl_3$) spectrum of reaction product (III)
Figure S11.6 ^{1}H-^{1}H COSY ($CDCl_3$, 500 MHz) spectrum of reaction product (III)
Figure S11.7 ^{1}H-^{13}C HSQC (125 MHz, $CDCl_3$) spectrum of reaction product (III)
Figure S11.8 ^{1}H-^{13}C HMBC (125 MHz, $CDCl_3$) spectrum of reaction product (III)

Circular Dichroism (CD) analysis

Figure S12.1 CD spectra of reaction substrate (I)
Figure S12.2 CD spectra of reaction product (III)

Scheme

(I) Product formation in the hydrogenation of linalool with 1%Ni-4%Pd/BC and 2%Ni-8%Pd/AC

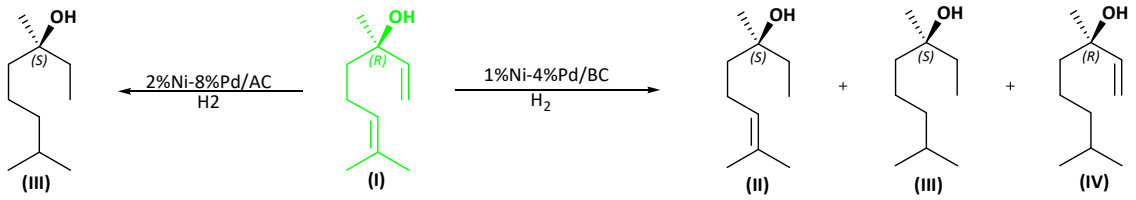

Figure S1

Experimental

Chemical and Reagents

(±)-Linalool, Pd $(NO_3)_2$, Ni $(NO_3)_2.6H_2O$, activated charcoal (AC), and all required chemicals and solvents were acquired from Sigma-Aldrich, Bengaluru. *Ocimum basilicum* variety CIM-Shishir plants were grown in CSIR-CIMAP, Lucknow research farm, Utter Pradesh, (Fig. S1). The aerial parts of CIM-Shishir were harvested and hydrodistilled for 3 to 4h by means of a Clevenger-types

apparatus for essential oil extraction[1]. The essential oil is saturated with anhydrous sodium sulphate and stored at 4 °C for further analysis.

Preparation of Biochar (BC) and Catalysts

Biochar (BC) was derived from the industrial waste of menthol mint (pitch). The material underwent pyrolysis at 500 °C for the duration of four hours in the inert atmosphere with heating rate 10 °C/min. For removal of inorganic residues, specifically ashes, the resulting biochar was treated with a 1M HCl solution and subjected to sonication for one hour at 40 °C. Following this treatment, the biochar was filtered and thoroughly rinsed with deionized water until a neutral pH was achieved. The final procedure involved oven drying of sample at 110 °C for 12 hrs. Additionally, varying percentages of palladium (Pd) and nickel (Ni) were incorporated into the synthesized biochar, zeolites, hydrotalcite (HT), and activated charcoal through a hydrothermal method, utilizing an aqueous solution of palladium nitrate ($Pd(NO_3)_2$) and nickel nitrate ($Ni(NO_3)_2$) as per our previously published methodology[2].

Characterization of Catalysts

The composites' X-ray diffraction pattern was attained using a Rigaku diffractometer (Rigaku, Japan), employing Cu Kα radiation at settings of 40 kV and 130 mA. These measurements covered a scan angle range from 5 to 90°, with a scanning speed of 0.05°. The resulting spectra are depicted as Intensity Vs 2θ. FT-IR spectra were verified on FT-IR spectrophotometer, Spirit QATR-S, by Shimadzu Japan. The samples were prepared using the KBr pellet technique, analysing a spectral range of 4000-500 cm-1 with a resolution of 4 cm^{-1}. Pellets were formed by thoroughly mixing 200 mg of dry KBr with 5 mg of the sample, followed by compressing under 10,000 hydraulic pressures for 2-3 min. For each sample, the spectrum was acquired over 200 scans, measuring the wave number against the percentage of transmittance. Thermogram profiles were studied using Mettler-Toledo TGA/DSC 1 Star system. For this, 5 mg sample was collected in a silica crucible, and the analysis was done in the following temperature program: 50-800 °C (10 °C/min) with a nitrogen flow rate of 40 mL/min as a purge gas. The obtained data were examined after obtaining the first derivative (DTG) to

ensure an unambiguous interpretation. The QUANTA-250, an FEI (Netherlands) SEM device, was employed for the morphological examination of the developed catalysts. Each sample, weighing 50 mg, was gold-coated by a Sputter Coater for the duration of 50 seconds (Model 147, Serial No: Q150 TES, frocoram Technology, U.K). To form layers on the substances, silver sputtering was applied. The equipment's settings were maintained at 30 kV to assess the size and form of the particles. The TEM analysis was conducted using an electron microscope equipped with filament to generate electrons, functioning at 300 kV. For TEM imagery and mapping, a Field Emission Gun-Transmission Electron Microscope 300 kV (specifically TEM 300 kV), from JOEL JEM 1400 was utilized.

The X-ray photoelectron spectroscopy (XPS) of all the samples was recorded using a Physics Electronics PHI 5000Verssa Probe III instrument.

The nitrogen adsorption isotherm is most frequently used technique for evaluating the porous characteristics of solid materials. The textural properties of all samples were resolved using N_2 adsorption isotherm measurements at 77K, which were conducted with automatic adsorption equipment (Quantachrome version 2.0 Instruments). Before carrying out the N_2 adsorption measurements, all samples were vented for 30 minutes under vacuum conditions at 120°C. The specific surface area (SSA) was estimated using the Brunauer–Emmett–Teller (BET) equation over a relative pressure (P/P_0) range of 0.05–0.35. To calculate the total pore volume, the liquid volumes of N_2 were determined based on amount adsorbed at high pressure. The distribution of pore sizes of all samples was resolved through the non-local density functional theory (NLDFT) equilibrium model.

Reaction Conditions

The produced catalysts were assessed for transformation of dihydrolinalool and tetrahydrolinalool from linalool. The procedure involved loading linalool with methanol, and placing it into a 25 mL capacity pressurized reactor. After that, catalyst was added at a specific ratio. The reaction mixture

was stirred at a temperature range of 120-180 °C for 60-180 min under constant hydrogen (H_2) pressure of 13.0 bar to achieve the desired product selectivity. After completion, the solution was filtered, and solvent was then eliminated using a BUCHI rotary evaporator at 45 °C under 160 mbar pressure.

The conversion of linalool and the selectivity of products during hydrogenation are determined according to Equations S1 and S2.

Equations S1

$$XCAL = \frac{Ccal^{o} - Ccal^{t}}{Ccal^{o}} \quad (1)$$

Where Ccal°= initial concentration, and Ccalt = concentration at time t

Product selectivity (Si) is calculated as

Equations S2

$$Si = \frac{Ci}{\sum Ci} \quad (2)$$

∑ Ci=total moles of product

Characterization of Ni-Pd/BC composite

In the XRD pattern, the Ni-Pd/BC composite displayed clear peaks corresponding to each element, as shown in Fig.1A. A broad diffraction peak positioned at 24.9° indicated the characteristic reflection of the amorphous carbon's "002" plane[3]. The XRD analysis revealed that both Pd and Ni-Pd/BC catalysts exhibited diffraction peaks at Bragg angle that matched the "111", "200", and "220" planes of Pd, located at angles of 40.1°, 46.7°, and 68°, respectively. This observed pattern aligned well with JCPDS No. 46-1043 standard crystallographic data, confirming presence of a face-centered cubic (fcc) structure within the Pd crystals. The diffraction peaks observed at 33.3° and 35.5° are attributed

to PdO as noted in JCPDS 00-041-1107, whereas the peaks appearing at 59.4° and 62.8° corresponded to NiO, referenced in JCPDS 73-1519[4]. However, the Pd signal was strong, thus, the Ni diffraction peak was relatively weak. This occurrence is associated with the BC's amorphous structure[5].

The spectra from FTIR are utilized to find functional groups present on catalysts surface (Fig.1B). The FTIR spectrum of the Ni–Pd/BC displayed a peak at 3633.92 cm^{-1}, which was attributed to –OH peak of water molecule. In addition, distinct peaks were observed at 1684.54 cm^{-1} and 1550.70 cm^{-1}, representing stretching vibrations absorption peak of C=C in the carbon skeleton. Furthermore, peak at 1369.35 cm^{-1} was credited to OH bending vibration of carboxyl group. The peaks at 1010.67 and 862.92 cm^{-1} were credited to C-O-C bond asymmetric stretching vibration. Lastly, stretching vibration of *cis*-epoxy ether bond gave peak at 748.0 cm^{-1}. It is noteworthy that O-H bending vibration peak in carboxyl group shifted to the high-frequency region at 1366.843 cm^{-1} after loading Pd–Ni[5]. The bands that overlap beneath 595.34 cm^{-1} are characteristic of metal-Oxygen vibrations, which may have arisen from the existence of NiO[6].

The thermal stability of pure carbon and Ni-Pd modified carbon are assessed using TGA (Fig.S2C). The modified catalyst exhibited minimal weight loss in comparison to pure carbon in the temperature range (50-800°C) studied, indicating the enhanced thermal stability of Ni-Pd/BC. Increasing metal loading was found to further improve thermal stability, possibly because of increased dispersion of Ni-Pd species over carbon surface.

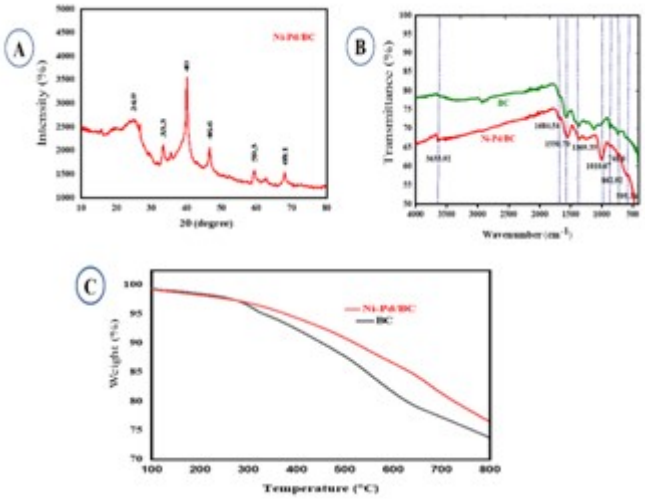

Figure S2 (A) XRD pattern, (B) FT-IR spectra, and (C) TGA curve of Ni-Pd/BC catalyst.

To evaluate the morphological analysis of BC and Ni-Pd/BC using SEM. SEM analysis revealed that both materials have distinct morphology as shown in Fig . S3 A and Fig. S3 B. These observations align well with the different background shapes of their XRD patterns, confirming the presence of NiO and Ni as well as PdO and Pd in the amorphous states on the catalyst surface. TEM images revealed that Ni and Pd were clearly visible in the imaging mapping region, indicating that Pd and Ni species were diffused over BC support surface, as shown in Fig. S3 C and Fig. S3 D, and further evaluated metals dopped percentage using SEM-EDS analysis (Fig. S3 E).

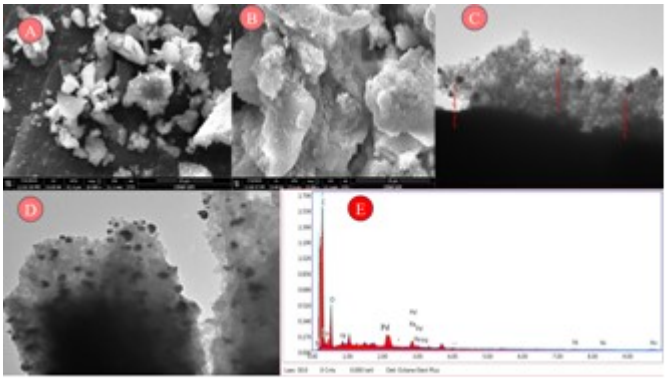

Figure S3 (A) SEM image of BC, (B) SEM image of 1%Ni-4%Pd/BC, (C and D) TEM image of 1%Ni-4%Pd/BC, and (E) EDS spectra of 1%Ni-4%Pd/BC.

The chemical characteristics of the bimetallic catalyst were evaluated through an XPS analysis. The XPS spectra for Pd 3d, Ni 2p, and C1s within catalysts are shown in Fig. S4 (A-D). The analysis of the Pd 3d level spectrum shows that it is composed of two spin-orbit-split doublets, equivalent to Pd $3d_{3/2}$ and Pd $3d_{5/2}$ species, with peaks observed at 333.5 and 338.8 eV, respectively, associated with metallic Pd $3d_{5/2}$ and Pd $3d_{3/2}$ orbits. In the case of Pd 2C, binding energy peaks at 335.8 and 341 eV are attributed to Pd $3d_{5/2}$ and Pd $3d_{3/2}$ orbits. The analysis of Ni 2p peaks in the catalyst reveals four distinct peaks at 854.2 eV for Ni (0) 2p3/2, 859.5 eV for Ni 2C $2p_{3/2}$, 871.6 eV for Ni (0) $2p_{1/2}$, and 878.1 eV for Ni 2C $2p_{1/2}$, indicating a contrast to the Ni values of 854.2 and 871.6 eV for Ni (0) $2p_{3/2}$ and $2p_{1/2}$, respectively. Furthermore, high-resolution C1s XPS spectra of the manufactured Ni-Pd/BC, as shown in Fig. 4B, reveal the principal component at 282.7 eV, indicative of carbon.

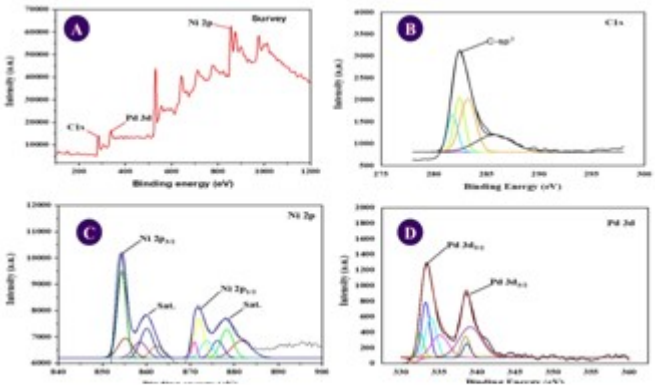

Figure S4 (A-D) XPS analysis of catalyst (1%Ni-4%Pd/BC), (A) XPS survey, (B) C1s binding state, (C) Ni 2p binding state (D) Pd 3d binding state

Characterization of Ni-Pd/AC Catalyst

The microstructural features of the Ni-Pd/AC were examined through XRD to gain an understanding of support materials crystallinity and phase transformations of Pd species (Fig. S5A). The XRD analysis showed unique patterns are essential for comprehending structural characteristics of catalysts. These patterns include broad, low-intensity peaks at a 2θ value of 24°, which is associated with the "002" plane of carbon. The broad and low-intensity characteristics of this peak indicated the amorphous quality of the carbon material, underscoring the absence of long-range crystalline organization commonly linked to graphitic structures. Additionally, the analysis identified distinct and pronounced peaks at 2θ values of 40°, 46°, and 68°, marked with diamonds.

These peaks correspond to the "111", "200", and "220" planes of metallic Pd species, respectively[7]. The "200", "220", and "311" planes all exhibit similar trends, confirmative of the fact that the catalysts are composed of Pd-Ni bimetals. Both samples displayed the characteristic "111", "200", and "220" reflections, which are indicative of the FCC crystal structure. As per the distinctive peak of the "111" plane, d-spacing values correspond to Pd-Ni [8]. The FT-IR spectra of Ni-Pd/AC are displayed in Fig. S5 B. The peak at 1694.9 and 1551.3 cm^{-1} is stretching vibration absorption peak of C=C in the AC skeleton. The spectral peak at 1044.4 cm^{-1} was credited to asymmetric stretching vibration of C-O-C as shown in Fig. S5 B. The thermal stability of AC and Ni-Pd/AC are assessed using TGA (Fig. S5 C). The catalyst exhibited minimal weight loss compared to AC in temperature

range studied (50-800 °C), indicating the enhanced thermal stability of the Ni-Pd/AC. Increasing metal loading was found to further improve thermal stability, possibly due to increased dispersion of Ni-Pd/AC species over carbon surface.

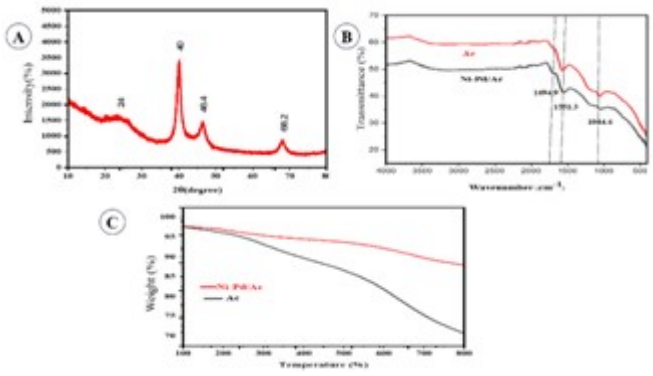

Figure S5 (A) XRD pattern, (B) FT-IR spectra, and (C) TGA curve of Ni-Pd/AC catalyst.

The morphological characteristics of support material and catalysts were assessed through SEM analysis (Fig S6A and S6B). The SEM images revealed that 2%Ni-8%Pd/AC has a textured surface, with small aggregated particles evident on catalyst's surface due to the presence of Ni and Pd. Furthermore, the SEM-EDS pattern confirms the successful integration of the doped metals (Ni and Pd) onto AC surface (Fig. S6E). The TEM images of prepared Ni-Pd/AC are shown in Fig. S6(C-D). The particle detected in whole imaging region of catalyst was clearly visible, indicating that Pd and Ni species were diffused over AC support surface.

The XPS measurement of Ni-Pd/AC catalyst was performed to investigate chemical bonding state and elemental composition. In resulting XPS survey spectrum (Fig. S7C), the distinct peaks corresponding to carbon, Ni, and Pd were observed, stating clear validation of their presence. The carbon peak representing C-sp3 was identified at a binding energy of 282.4 eV (Fig. S7A). The Pd binding energy of 337.8 eV (Pd^0, $3d_{5/2}$) and 343.1 eV (Pd^0, $3d_{3/2}$) are obtained, while 333.5 eV (Pd^{2+}, $3d_{5/2}$) and 338.9 eV ($Pd^{2+,}$ $3d_{3/2}$) are assigned to Pd^{2+} in the catalysts (Fig. S7B)[9]. However, the Pd signal was strong, thus, the Ni diffraction peak was relatively weak. This occurrence is associated with the AC's amorphous structure and Ni peak not observed in AC support material[5].

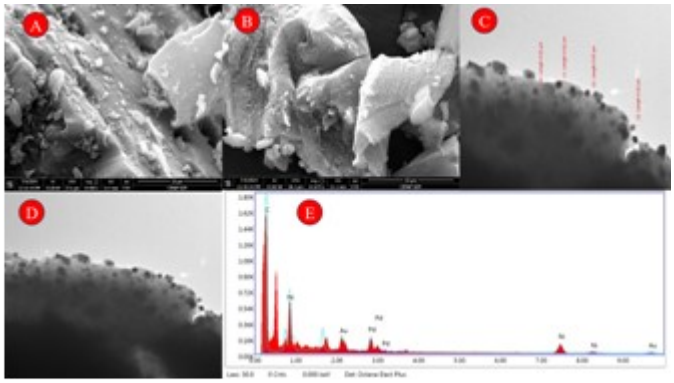

Fig. S6 (A) SEM image of AC, (B) SEM image of 2%Ni-8%Pd/AC, (C and D) TEM image of 2%Ni-8%Pd/AC, and (E) EDS spectra of 2%Ni-8%Pd/AC

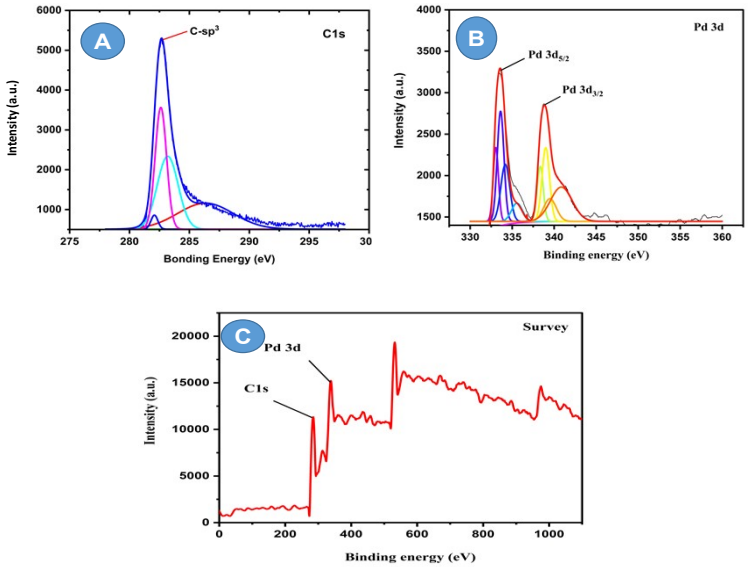

Fig. S7 (A-C) XPS analysis of 2%Ni-8%Pd/AC, (A) C1s binding states, (B) Pd 3d binding states, and (C) XPS survey spectrum of catalyst

Characterization of Surface area and porosity

To determine physical properties like surface area, pore volume, and porosity, Brunauer-Emmett-Teller (BET) surface area analysis was accomplished on all samples. The calculated surface areas were as follows: 24.6 m^2/g for biochar (BC), 37.7 m^2/g for Ni-Pd/BC, 998.9 m^2/g for activated charcoal (AC), and 805.3 m^2/g for Ni-Pd/AC. Additionally, all samples were found to be porous in nature. The average pore size is observed as 3.169 nm and 3.797nm for biochar and Ni-Pd/BC, respectively, whereas activated charcoal (AC) and Ni-Pd/AC have the same pore size of 1.475 nm.

Further pore size nature of all materials is defined by non-local density functional theory (NLDFT) equilibrium approaches. Table S1 represents **t**he pore diameter indicated that Biochar (BC) and Ni-Pd/BC are mesoporous whereas Activated charcoal (AC) and Ni-Pd/AC are microporous materials[10].

The pore volumes of BC, Ni-Pd/BC, AC, and Ni-Pd/AC are 0.025, 0.100, 0.455, and 0.533 cm^3/g, respectively. The isotherm (adsorption-desorption) was obtained through N_2 adsorption at 77K (**Fig. S8**). The isotherm of Ni-Pd/BC and Ni-Pd/AC belongs to Type IV, whereas the isotherm of biochar (BC) belongs to Type I and isotherm of Activated charcoal (AC) belongs to Type II[11]. The average pore size indicates that BC and Ni-Pd/BC possess mesoporous characteristics, while AC and Ni-Pd/Ac exhibit microporous properties. This observation aligns well with the porosity findings derived from the TEM images. The specific surface area of Ni-Pd/BC has shown an increase compared to BC, whereas Ni-Pd/AC has exhibited a decrease in surface area relative to AC. The observed increase in surface area and pore volume of BC after modification with metals can be attributed to the creation of additional mesoporous and improved pore accessibility during metal incorporation and thermal treatment. This hydrogenation may be credited to obstruction of numerous micropores caused by Ni-Pd metals.

Table S1: Characterization of Surface area and porosity

Samples	Surface area ($m^2\ g^{-1}$)	Pore volume ($cm^3\ g^{-1}$)	Pore width (nm)
Biochar (BC (AB01)	24.6	0.025	3.169
Ni-Pd/BC (AB02)	37.7	0.100	3.794
Activated Charcoal (AC)(AB03)	998.9	0.455	1.475
Ni-Pd/AC (AB04)	805.3	0.533	1.475

Additionally, surface area of Ni-Pd/AC decreases as average pore size increases. This is credited that crystallinity and particle size are inversely related to surface area. X-ray diffraction (XRD) analysis indicates that both AC and Ni-Pd/AC exhibit a largely amorphous structure, which can be linked to their smaller particle sizes. AC and Ni-Pd/AC show elevated levels of surface area, pore volume, and

porosity. These materials exhibit significant adsorption capacity, rapid adsorption rates, thermal stability, and relative simplicity in terms of regeneration. Additionally, they possess good chemical stability. As a result, the Ni-Pd/AC composite effectively reduces linalool to tetrahydrolinalool. In contrast, both BC and Ni-Pd/BC have a lower surface area, pore volume, and porosity, with the Ni-Pd/BC composite reducing linalool to dihydrolinalool. According to IUPAC, in the realm of physisorption, pore sizes are categorized into three groups: (i) micropores, which are up to around 2 nm in size, (ii) mesopores, which range from 2-50 nm, and (iii) macropores, which are larger than approximately 50 nm or 0.05 μm[12].

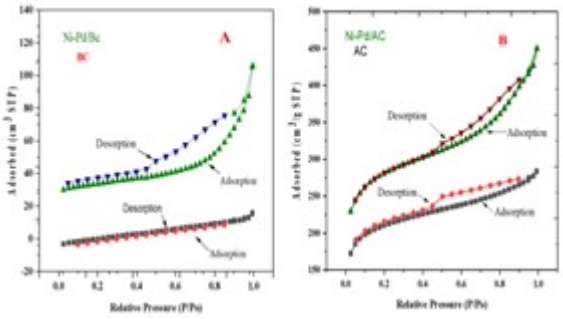

Figure S8. N_2 isotherm (adsorption-desorption) of base materials and catalysts at 77K

Reusability of Catalysts

The reusability of 1%Ni-4%Pd/C and 2%Ni-8%Pd/AC catalysts was thoroughly assessed via multiple continuous processes. After each process cycle, the catalysts were rigorously washed to remove any adsorbed materials and then calcined at 450°C to restore their activity. This regeneration process ensured that the catalysts maintained their structural integrity and catalytic performance. The reusability data demonstrated that the conversion rates and selectivity towards the desired products, dihydrolinalool, and tetrahydrolinalool, remained consistently high even in five consecutive runs (**Fig. S9**). This stability highlights the robustness and efficiency of 1%Ni-4%Pd/C and 2%Ni-8%Pd/AC catalysts in promoting the desired chemical reactions without significant loss of activity, making them viable for long-term industrial applications.

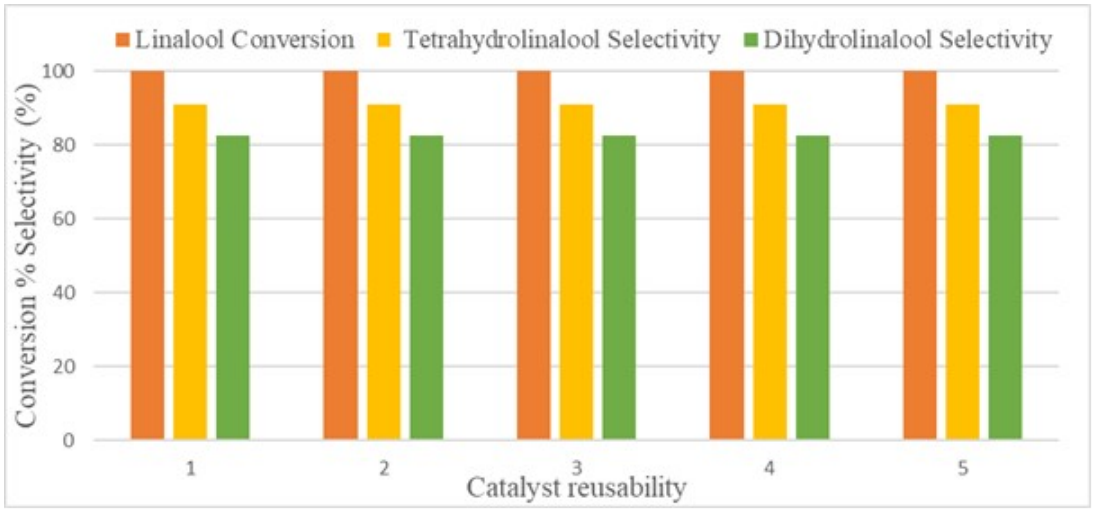

Figure S9 Reusability investigation of composites 1% Ni-Pd 4%P/BC for dihydrolinalool & 2%Ni-8%Pd/AC for tetrahydrolinalool

Valorisation of *Ocimum basilicum* variety CIM-Shishir Essential Oil

The optimized conditions for the synthesis of 6,7-dihydrolinalool (II) and tetrahydrolinalool (III) have been directly applied to the linalool rich essential oil and obtained almost similar results.

The *Ocimum basilicum* variety CIM-Shishir essential oil is composed of linalool (75.2%; I), camphor (8.6%), 1,8-cineole (5.6%), and limonene (1.1%). When CIM-Shishir essential oil was hydrogenated using a 1%Ni–4%Pd/BC and transformed linalool (75.2%) in essential oil into 63.5% 6,7-dihydrolinalool (II) (>84% selectivity), 6.6% 1,2-dihydrolinalool (IV) and 5.6% tetrahydrolinalool (III) with complete conversion of linalool.

Similarly, Further, *Ocimum basilicum* essential oil (75.2% linalool; I) modified with 2%Ni-8%Pd/AC into tetrahydrolinalool 68.9% (>91% selectivity; III) along with 2.7% 1,2-dihydrolinalool (IV) with >98% conversion of the reaction substrate. The comparative chemical compositions of pure and modified essential oils are shown in Table S2. In addition, the Total ion chromatogram (TIC) recorded using a GC-MS of both pure and modified essential oils are also given, separately (**Fig. S10.5 and Fig. S10.6**). The catalytic outcomes of pure substrate (I) and in CIM-Shishir essential oil revealed the efficiency of the process.

Table S2 Chemical compositions of pure and modified essential oils of *O. basilicum* var. CIM-Shishir

Constituents	**RI[a]**	**RI[b]**	**CIM-Shishir oil**	**Hydrogenated Shishir oil with 2%Ni-8%Pd/AC**	**Hydrogenated Shishir oil with 1%Ni-4%Pd /BC**	IM
α-Pinene	934	932	0.2	0.1	-	a,b
Camphene	949	946	0.8	0.2	-	a,b
Sabinene	973	969	0.3	0.1	-	a,b
β-Pinene	978	974	0.7	0.1	-	a,b
β-Myrecene	990	986	0.7	0.1	-	a,b
Limonene	1029	1026	1.1	-	-	a,b
1,8-Cineole	1031	1030	5.6	5.6	4.5	a,b
(*E*)-β-Ocimene	1046	1044	0..4	-		a,b
γ- Terpinene	1058	1054	0.2	-		a,b
Terpinolene	1089	1086	0.2	-	0.1	a,b
Tetrahydrolinalool (III)	-	1098	-	68.9	5.6	a,b,c
Linalool (I)	1096	1102	75.2	nd	nd	a,b,c
1,2-Dihydrolinalool (IV)	-	1120	-	2.7	6.6	a,b,
6,7-Dihydrolinalool (II)	-	1135	-	-	63.5	a,b,c
Camphor	1146	1145	8.6	10.1	8.8	a,b
Borneol	1167	1165	0.2	0.2	0.1	a,b
Terpinen-4-ol	1178	1174	0.3	-	0.4	a,b
α- Terpineol	1191	1189	0.4	-	0.5	a,b
Methyl Chavicol	1199	1195	0.6	0.5	0.3	a,b
Bornyl acetate	1287	1285	0.2	0.2	0.2	a,b
Eugenol	1358	1356	0.1	-	0.1	a,b
α- Copaene	1377	1374	-	0.2	0.1	a,b
β-Cubenene	1386	1386	-	-	0.1	a,b
β- Elemene	1391	1389	-	0.3	0.1	a,b
β-Caryophyllene	1421	1418	-	0.2	0.2	a,b
(*Z*)-β-Farnescene	1440	1440	-	0.3	0.1	a,b
α- Humulene	1455	1454	0.1	0.3	0.2	a,b
(*E*)-β-Farnescene	1458	1458	-	0.3	tr	a,b
Germacrene D	1482	1482	0.7	0.1	nd	a,b
Bicyclogermacrene	1498	1500	0.2	0.2	nd	a,b
Germacrene A	1507	1507	0.2	0.2	nd	a,b
δ- Cadinene	1515	1513	0.2	0.2	0.1	a,b
1,10-di-epi-Cubenol	1616	1612	-	0.2	0.5	a,b
Epi-α-Cubenol	1642	1638	0.4		0.7	a,b

a; Retention index, b; Mass-spectrometry based detection, c; NMR based identification. All the presented data are validated through standard deviation. RI[a]: Reported retention index by Dr. RP Adams, 2017 edition 4. 1. RI[b]: Calculated Retention Index in ELITE-5 capillary columns using a homologous series of *n*-alkanes (C_7-C_{30} hydrocarbons), tr; trace < 0.1%, nd; not detected. All the data was reported along with their standard deviation (sd).

Circular Dichroism (CD) Measurement of Linalool and its Derivatives

Since linalool (I) and tetrahydrolinalool (III) are optically active molecules. Thus, we have studied their optical activity using CD spectrophotometer system. A thorough analysis revealed that linalool and tetrahydrolinalool showed CD (millidegree) at 220 nm and 280 nm, respectively (**Fig. S14.1 and Fig. S14.2**). Moreover, we conclude that linalool absorbed the left-handed circularly polarized light (L-CP) to a reduced extent than right-handed circularly polarized light (R-CP). Therefore, CD signal of linalool appears as negative. On the other hand, tetrahydrolinalool showed positive signal due to absorption of right-handed circularly polarized light (R-CP).

Methods of separation and purification, and the analytical and quantitative techniques applied to the reaction products

The reaction product was subjected to column chromatography, using a 230-400 mesh silica gel (Merck) for compound purification. Diethyl ether and distilled hexane were used as the mobile phase. A paste by combining 1.0 mL of catalytically modified oil with 5 g of silica gel was prepared, which was then loaded onto the column having 15g of silica. The polarity of the mobile phase was progressively raised from 100% hexane to 15% diethyl ether. A total of 130 fractions were collected in 10 mL volume tube. Thereafter the column was washed with 100% ethyl acetate and terminated (Scheme I). After TLC pattern and quantitative GC-FID analysis, pooled fraction #16-31 as compound (II) and pooled fraction #31-40 as compound (III) were subjected to mass spectrometry and NMR analysis.

Scheme I: Flowchart of separation and purification of the reaction products

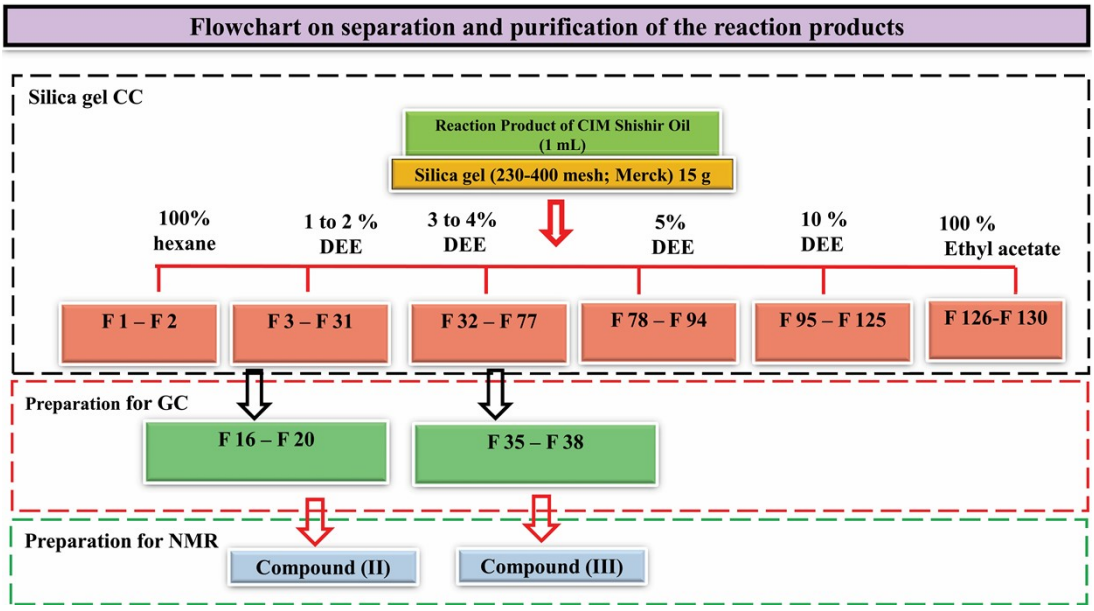

Circular Dichroism (CD) spectroscopy

Circular Dichroism (CD) spectra of compound (I) and compound (III) were measured using a J-1500 CD spectrometer (JASCO) for the purpose of determining the stereochemistry of (I) and tetrahydrolinalool (III). For the CD spectra, 1mm path length quartz cell was used, with bandwidth of 1 nm. A concentration of 10 mg/ml of compound (I) and compound (III) were dissolved in methanol, and spectra were recorded at 100 nm min^{-1} scan speed, an average of 3 accumulations in the measuring range 400-190 nm scale.

GC-FID and GC-MS Analysis of Reactant and its Derivatives

The chemical composition pure substrate, hydrogenated reaction products, crude essential oil and hydrogenated CIM-Shishir essential oil was investigated by using a Varian make (CP 3800) gas chromatography system equipped with a Flame Ionization Detector (FID). Varian CP 3800 gas chromatography system configured with a 30 meter long non-polar fused silica column (internal diameter of 0.25 mm and 0.25 µm film thickness, PerkinElmer make Elite-5) was programmed with 60 °C initially with an increase of 3 °C/min to 240 °C. With a final ramp rate of 10 °C/min, with a

final hold time of 1 minute, the final oven column temperature of 310 °C was achieved. The split ratio was set as 1:100 for split/splitless injector kept at 300 °C using hydrogen as the carrier gas at a constant flow rate of 1 mL/min. The gas chromatographic detector (FID) temperature was maintained at 300 °C for the entire analysis as per reported method.

For GC-MS analysis, a Clarus 680 GC system equipped with a Clarus SQ 8C Quadrupole mass spectrometer (Perkin Elmer) was used, employing an Elite-5 MS capillary column (30 x 0.25 mm x 0.25 µm) to confirm the compound identity. Helium served as the carrier gas at a constant flow rate of 1 mL/min, and electron ionization was performed at 70 eV . The identification of components within the pure and hydrogenated essential oils was achieved using retention index (RI) calculated with reference to the retention time of straight chain normal alkane mixture ranged from C_7 to C_{30} (the certified reference material: C_7-C_{30} hydrocarbons, Sigma-Aldrich; 49451-U), and by mass spectral comparison against the integrated NIST 2011 (ver 2.3.0) and Wiley library databases, and published literature on essential oil[13].

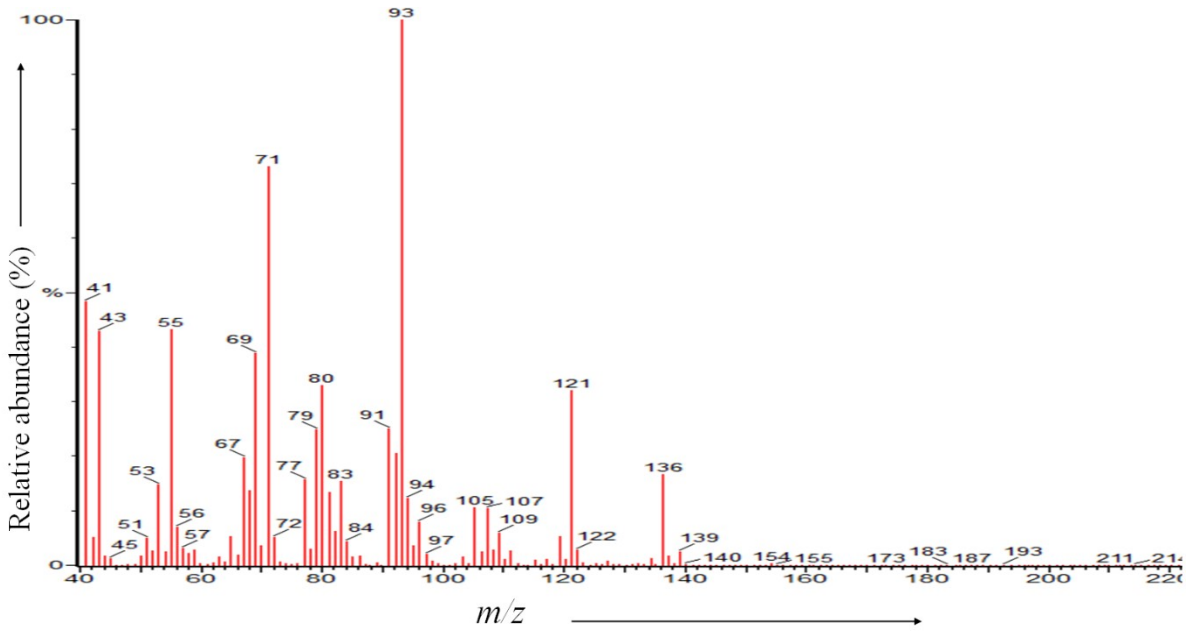

Figure S10.1 Mass spectrum of reaction substrate (I)

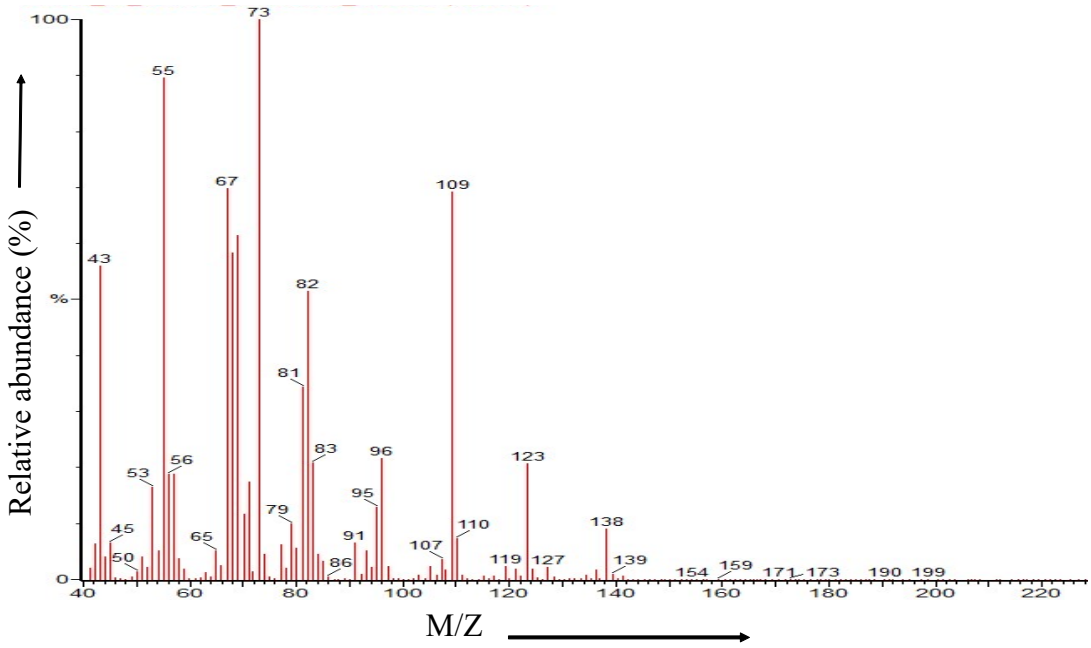

Figure S10.2 Mass spectrum of reaction product (IV)

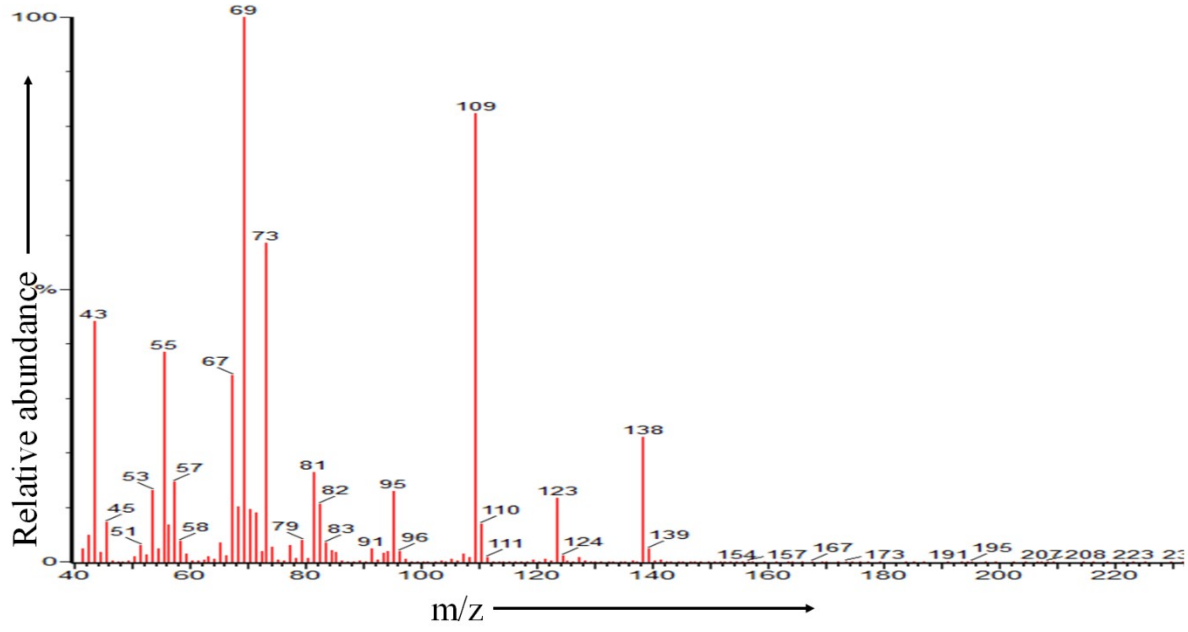

Figure S10.3 Mass spectrum of reaction product (II)

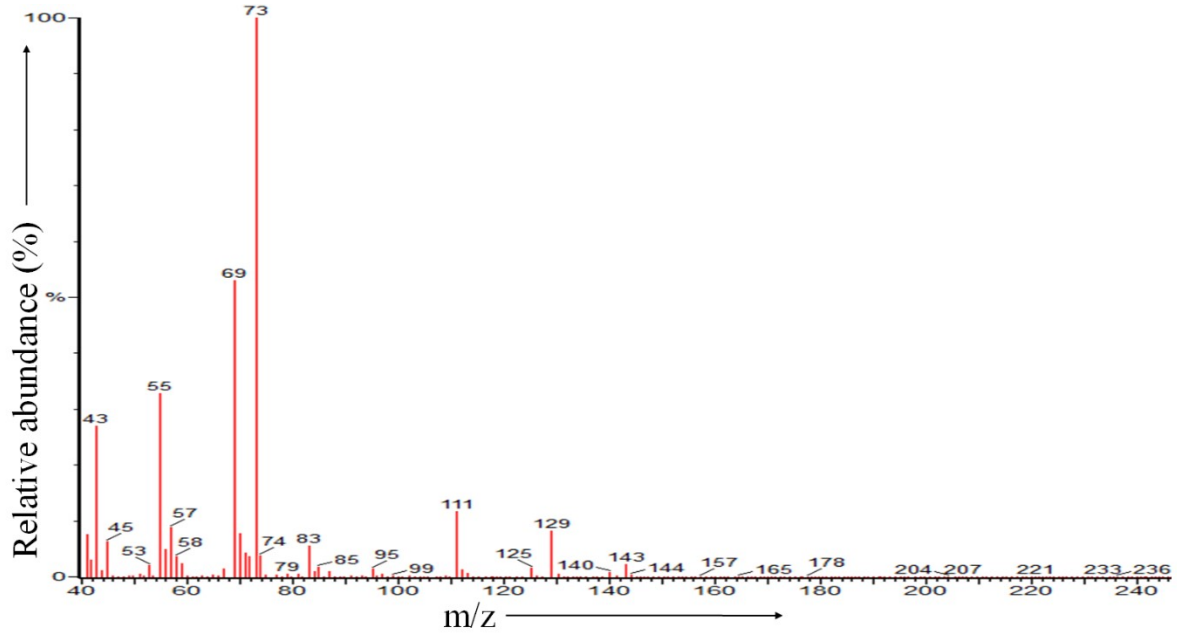

Figure S10.4 Mass spectrum of reaction product (III)

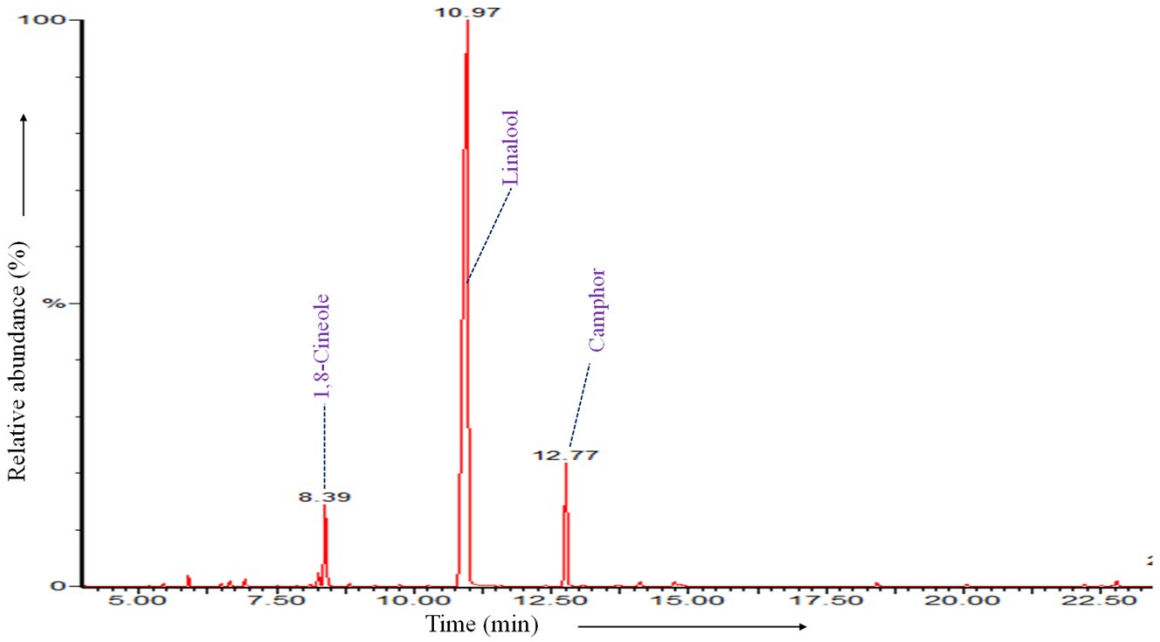

Figure S10.5 Total ion chromatogram of essential oil extracted from aerial parts of *Ocimum basilicum* variety CIM-Shishir essential oil

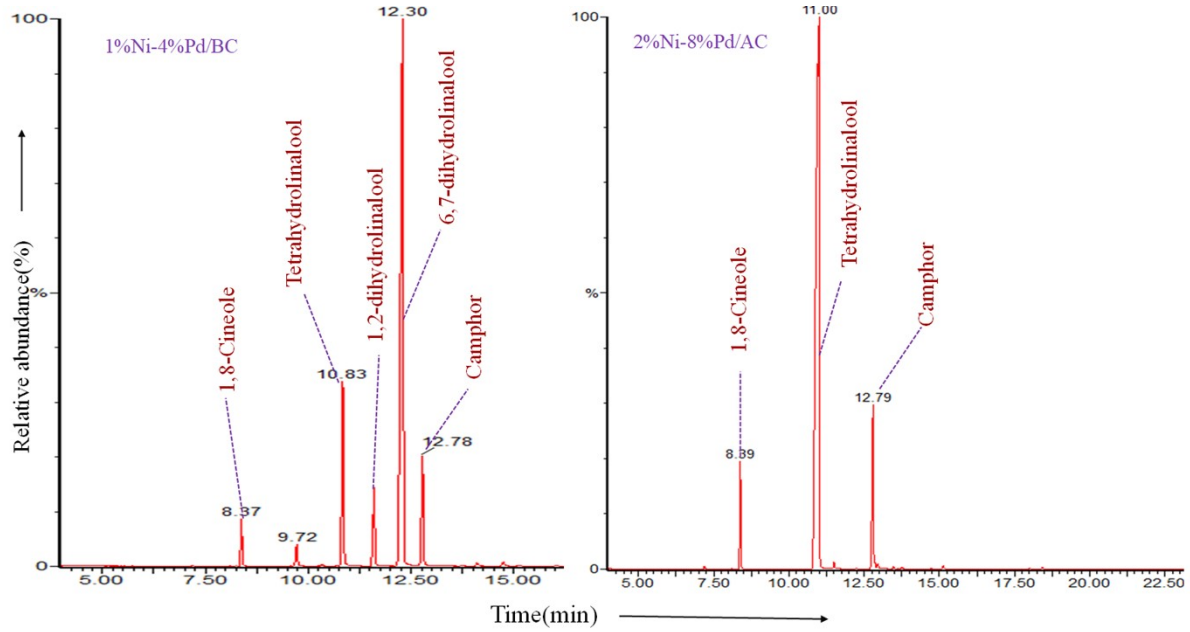

Figure S10.6 Total ion chromatogram of modified essential oils with 1%Ni-4%Pd/BC and 2%Ni-8%Pd/AC

NMR data of reaction substrate and Products

A series of NMR experiments (BrukerBiospin GmbH, Germany, 500 MHz (B0=11.75 T) have been recorded using a Bruker Avance-III HD Spectrometer. For one-dimensional ^{1}H- and ^{13}C NMR measurements, a chemical shift value (0.00 δ ppm) of TMS (tetramethylsilane) was taken as a reference. In addition, chemical shifts (ppm units) of deuterated solvent (chloroform-d, $CDCl_3$) were set to 7.26 for 1H- and 77.0 for 13C-NMR experiments. The 2-dimensional NMR experiments like 1H -1H COSY, Heteronuclear Single Quantum Coherence (HSQC), Heteronuclear Multiple Bond Correlation (HMBC), etc. were also recorded. A clear solution of about 20 mg of neat sample was prepared in deuterated solvent ($CDCl_3$) and subjected to NMR resonance measurement using a 5 mm NMR tube. Multiplicity is shown as; s, singlet; d, doublet; t, triplet; q, quartet; m, multiplet; br, broad) using the published protocol

After the reaction, the solvent was evaporated under vacuum on a rotary evaporator (40°C, 160 mbar) and obtained products. For the structure elucidation of the reaction products, and substrate, detailed NMR investigations have been carried out. For comparison, the NMR spectra compounds such as linalool (I), 6,7-dihydrolinalool, (II), and tetrahydrolinalool (III) were given below:

Linalool (I)

^{1}H NMR ($CDCl_3$): δ 5.93-587 (1H, m, H-2), 5.22-5.05 (2H, m, H-1), 5.11-5.09 (1H, m, H-6), 2.03-1.98 (2H, m, H-5), 1.67 (3H, s, H-9), 1.59 (3H, s, H-8), 1.58 (2H, m, H-4), 1.27 (3H, s, H-10);

^{13}C NMR ($CDCl_3$): δ 145.03 (C-2), 131.96 (C-7), 124.31 (C-6), 111.69 (C-1), 73.49 (C-3), 42.4 (C-4), 27.86 (C-10), 25.5 (C-10), 25.7 (C-9), 22.8 (C-5), 17.69 (C-8);

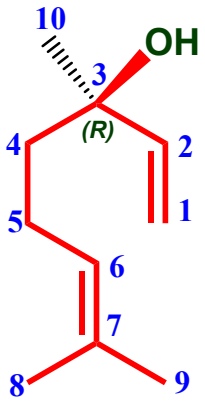

6,7-dihydrolinalool (II)

^{1}H NMR ($CDCl_3$): δ 5.13-5.11 (1H, t, H-6), 2.05-2.0 (2H, m, H-5), 1.68 (3H, s, H-9), 1.61 (3H, s, H-8), 1.49 (2H, m, H-2), 1.47 (2H, m, H-9), 1.15 (3H, s, H-10), 0.9 (3H, m, H-1),

^{13}C NMR ($CDCl_3$): δ 131.72 (C-7), 124.51 (C-6), 72.99 (C-3), 41.55 (C-4), 34.23 (C-2), 26.26 (C-10), 25.73 (C-9), 22.63 (C-5), 17.65 (C-8), 8.25 (C-1);

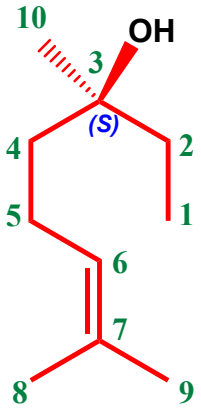

Tetrahydrolinalool (III)

^{1}H NMR ($CDCl_3$): δ 1.55-1.53 (1H, m, H-7), 1.47 (2H, m, H-2), 1.40-1.38 (2H, m, H-4), 1.30-1.28 (3H, m, H-5), 1.16-113(2H, m, H-6), 0.87 (3H, s, H-8), 0.87 (3H, s, H-9), 0.86 (3H, m, H-1),

^{13}C NMR ($CDCl_3$): δ 72.92 (C-3), 41.60 (C-4), 39.58 (C-6), 34.25 (C-2), 27.94 (C-7), 26.38 (C-10),

22.59 (C-8), 22.59 (C-9), 21.58 (2H, m, H-5), 8.16 (C-1);

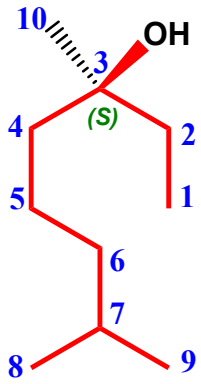

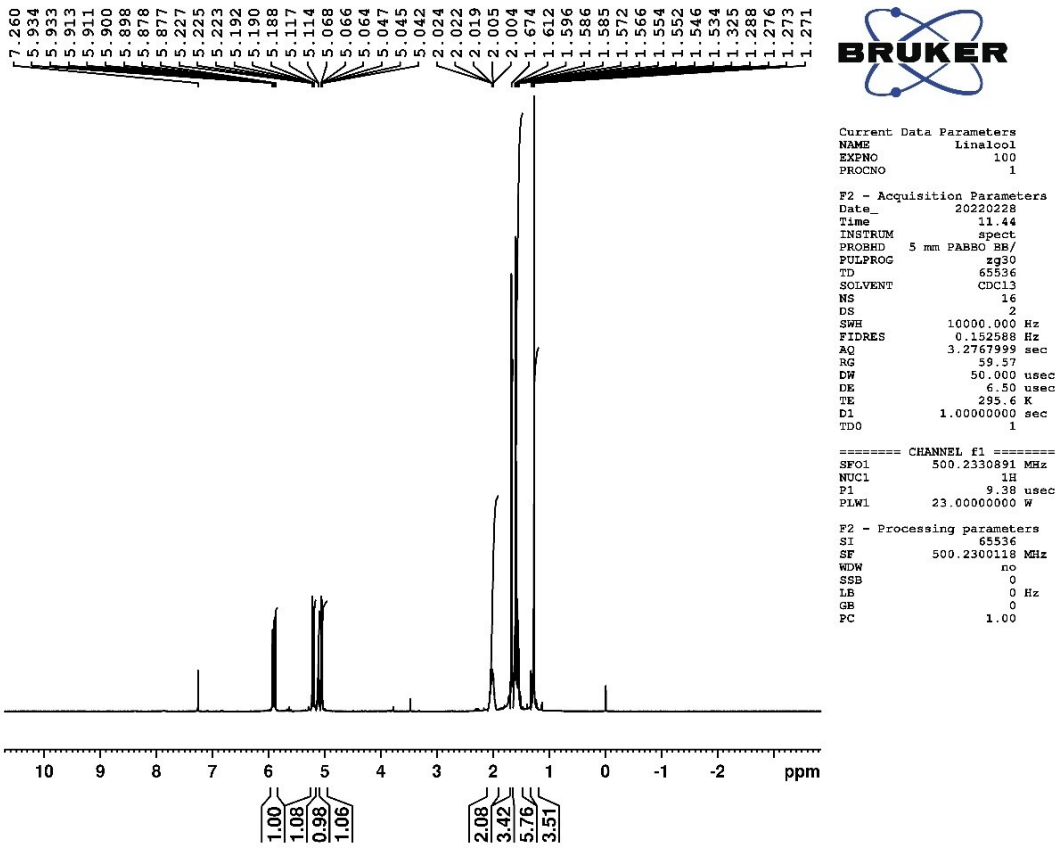

Figure S11.1 ^{1}H-NMR (500 MHz, $CDCl_3$) spectrum of reaction substrate (I)

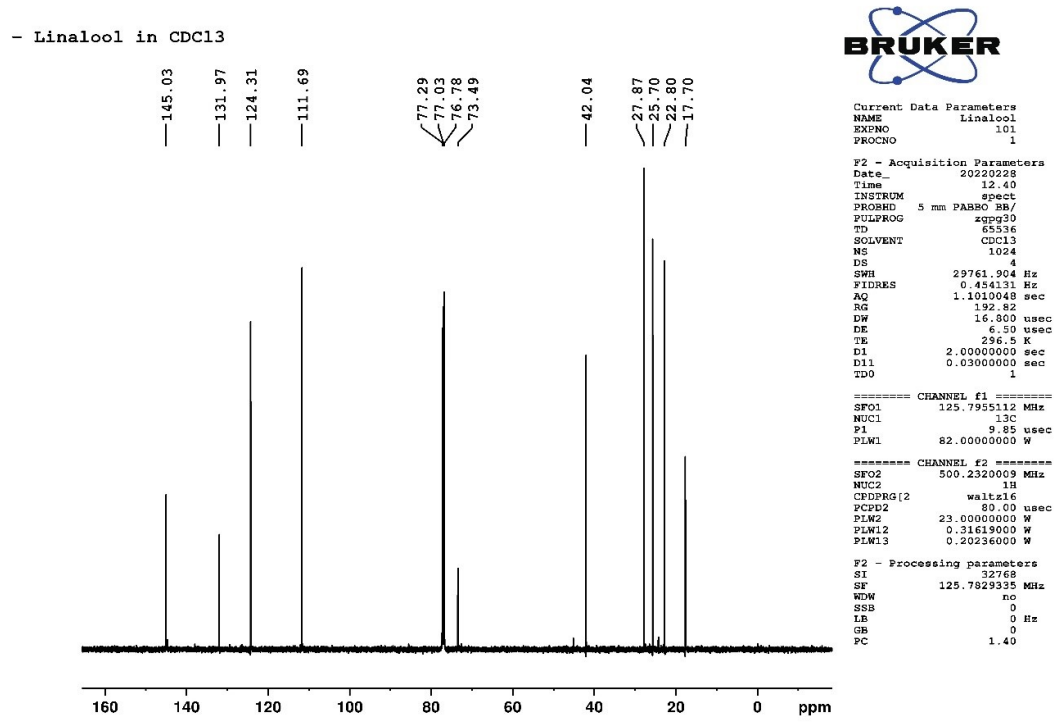

Figure S11.2 ^{13}C-NMR (125 MHz, $CDCl_3$) spectrum of reaction substrate (I)

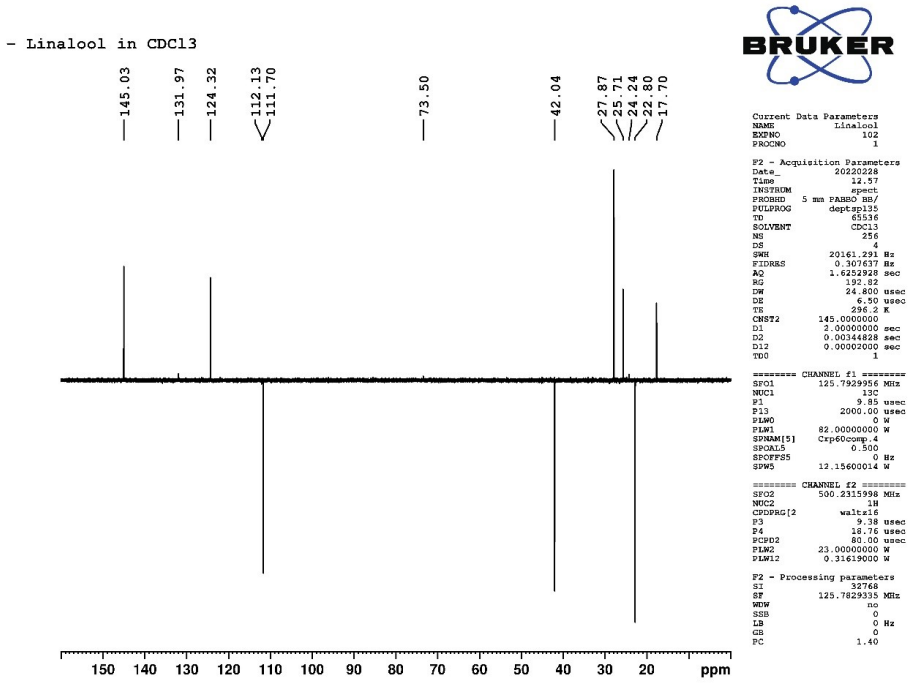

Figure S11.3 DEPT 135° (125 MHz, $CDCl_3$) spectrum of reaction substrate (I)

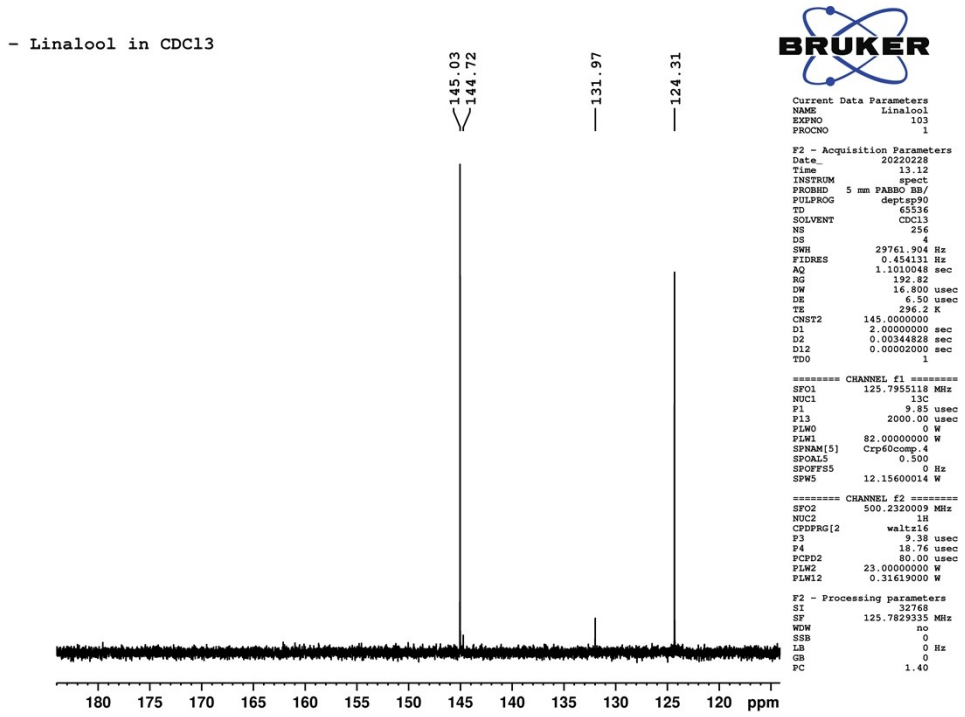

Figure S11.4 DEPT 90° (125 MHz, $CDCl_3$) spectrum of reaction substrate (I)

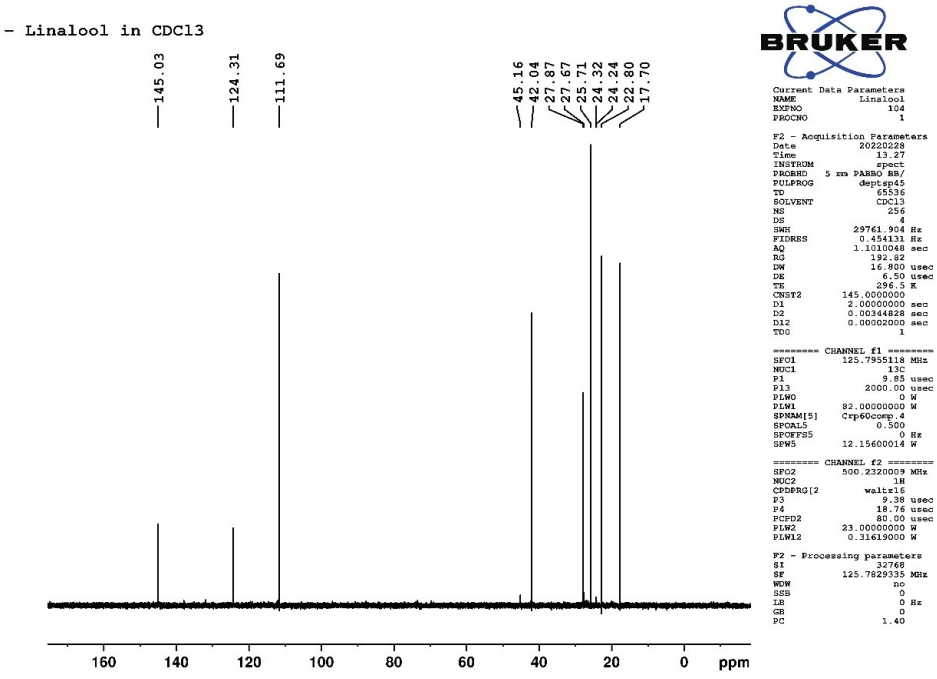

Figure S11.5 DEPT 45° (125 MHz, $CDCl_3$) spectrum of reaction substrate (I)

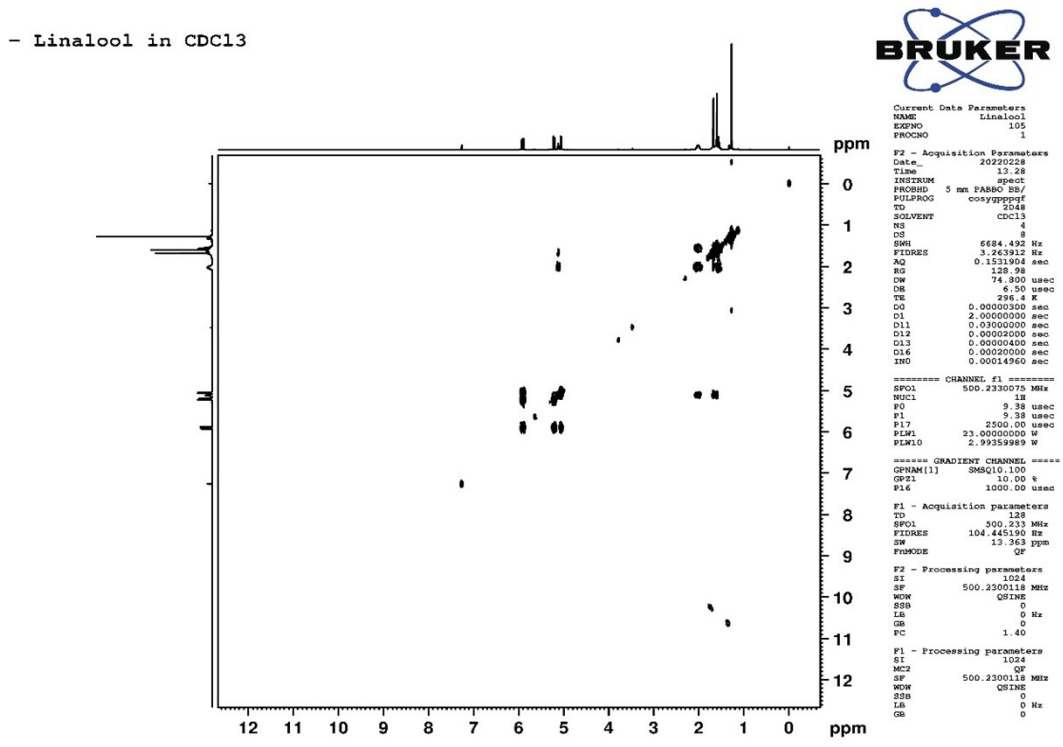

Figure S11.6 1H-^{1}H COSY ($CDCl_3$, 500 MHz) spectrum of reaction substrate (I)

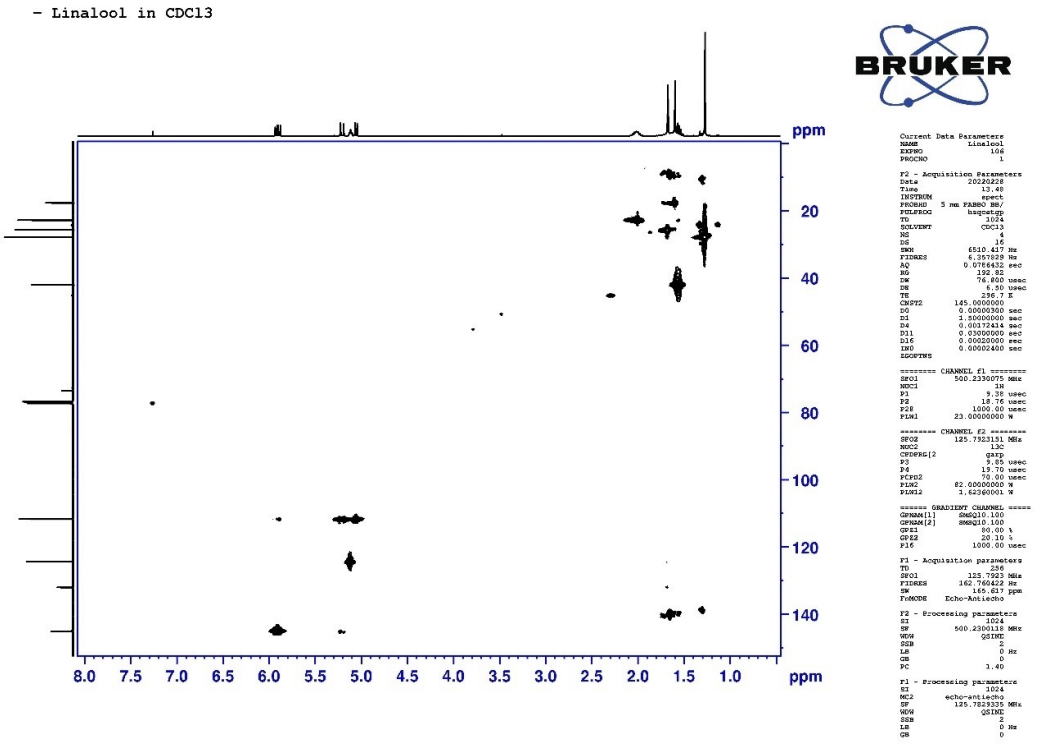

Figure S11.7 ^{1}H-^{13}C HSQC (125 MHz, $CDCl_3$) spectrum of reaction substrate (I)

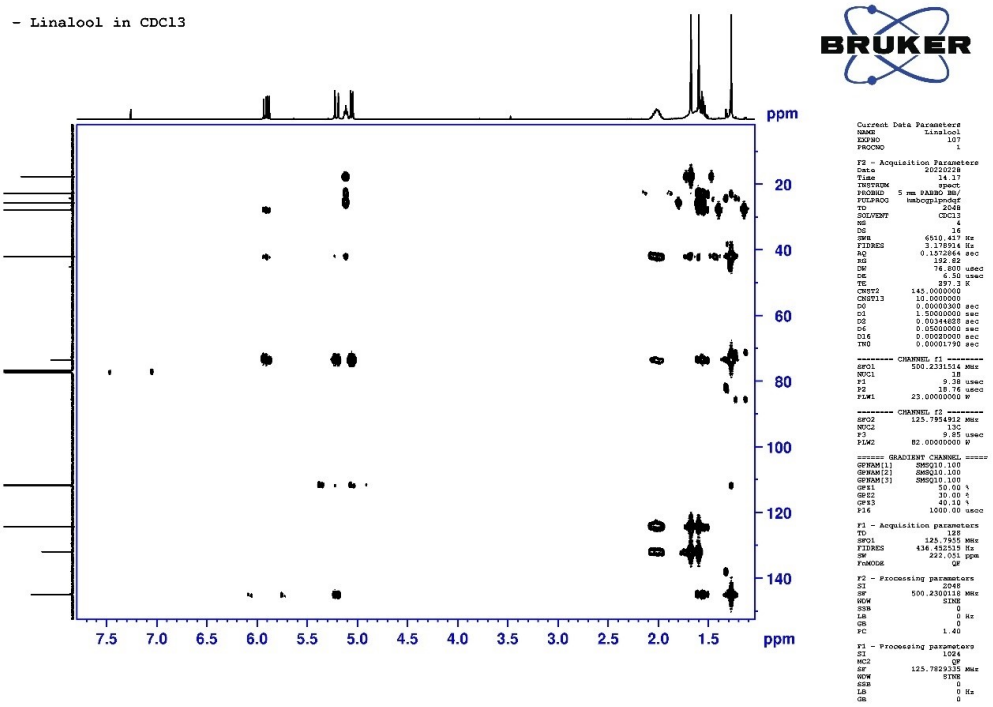

Figure S11.8 ^{1}H-^{13}C HMBC (125 MHz, $CDCl_3$) spectrum of reaction substrate (I)

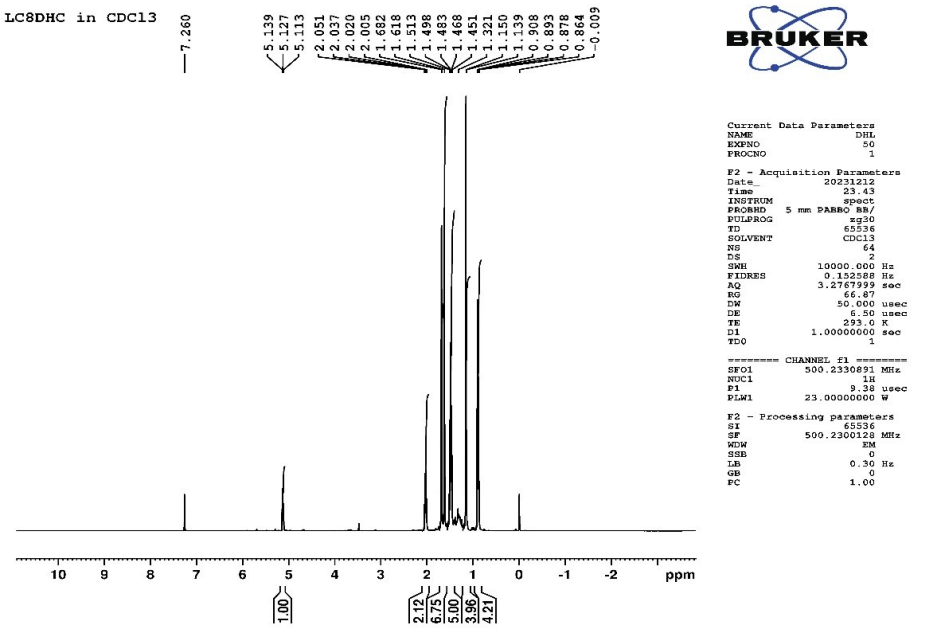

Figure S12.1 ^{1}H-NMR (500 MHz, $CDCl_3$) spectrum of reaction product (II)

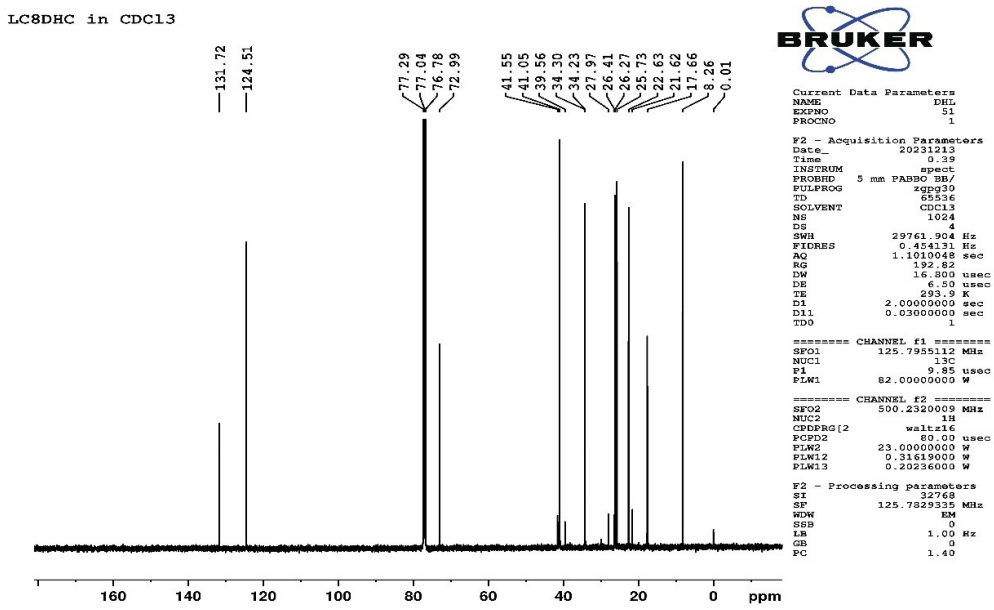

Figure 12.2 ^{13}C-NMR spectrum of reaction product (II)

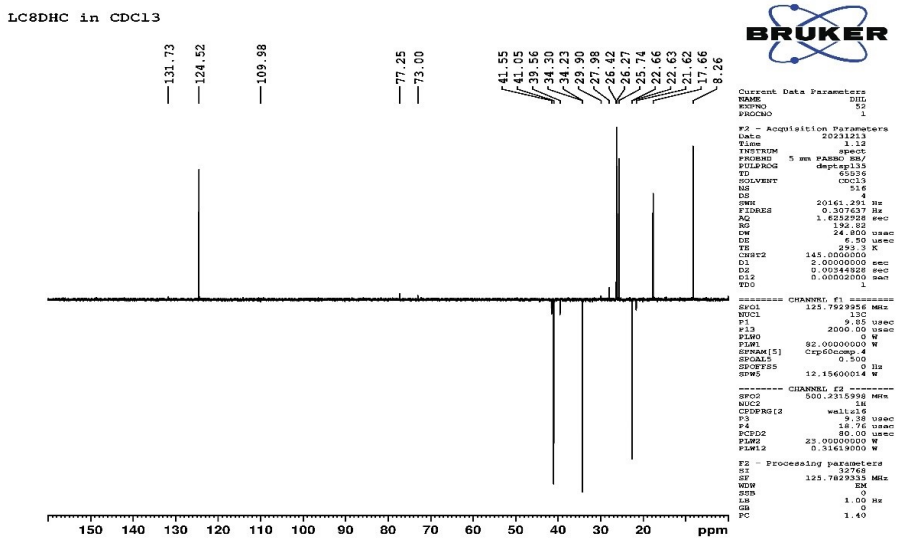

Figure S12.3 ^{13}C NMR DEPT 135° spectrum of reaction product (II)

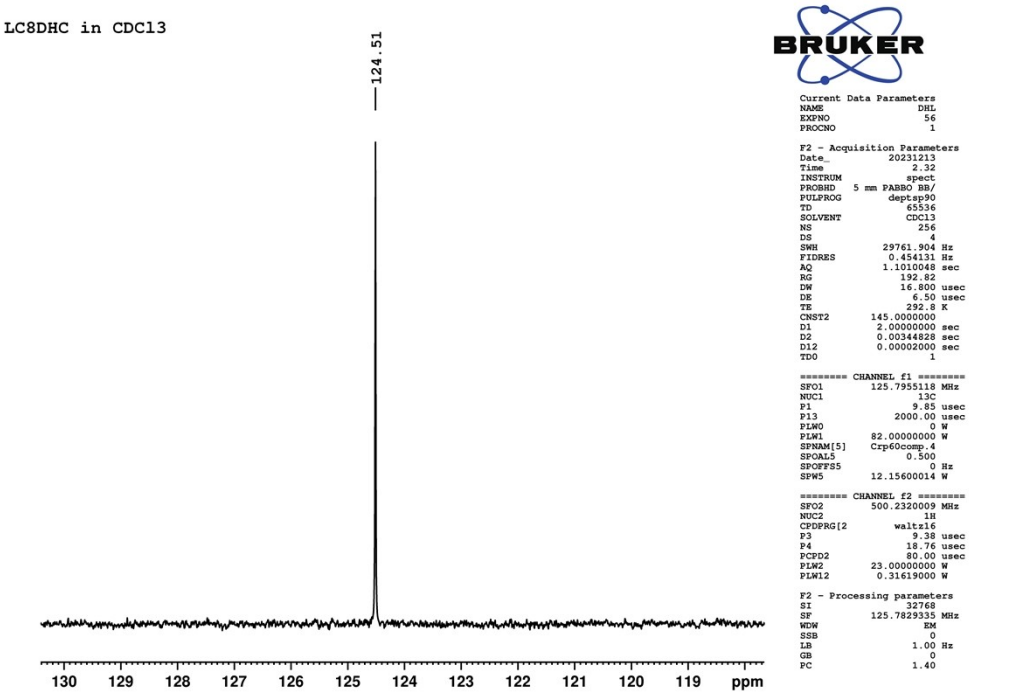

Figure S12.4 DEPT 90°spectrum of reaction product (II)

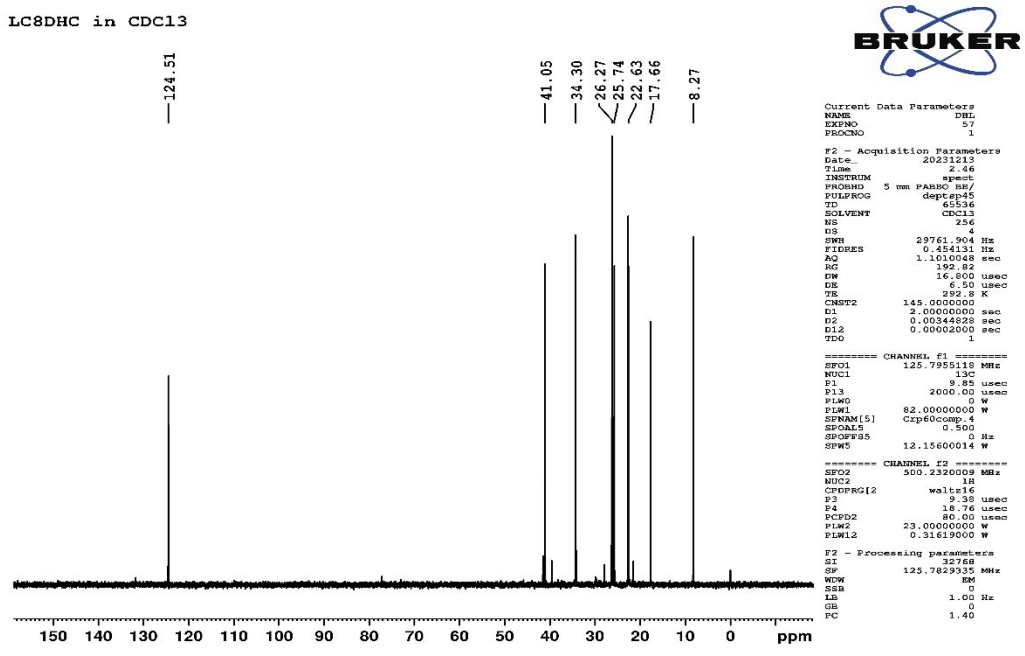

Figure S12.5 DEPT 45° spectrum of reaction product (II)

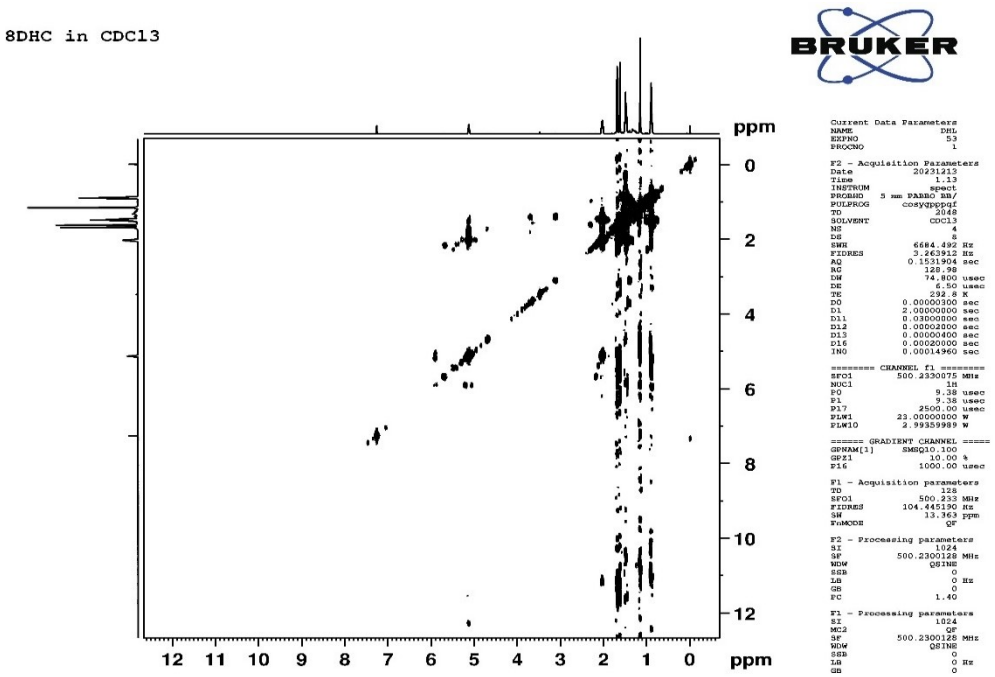

Figure S12.6 ^{1}H-^{1}H COSY spectrum of reaction product (II)

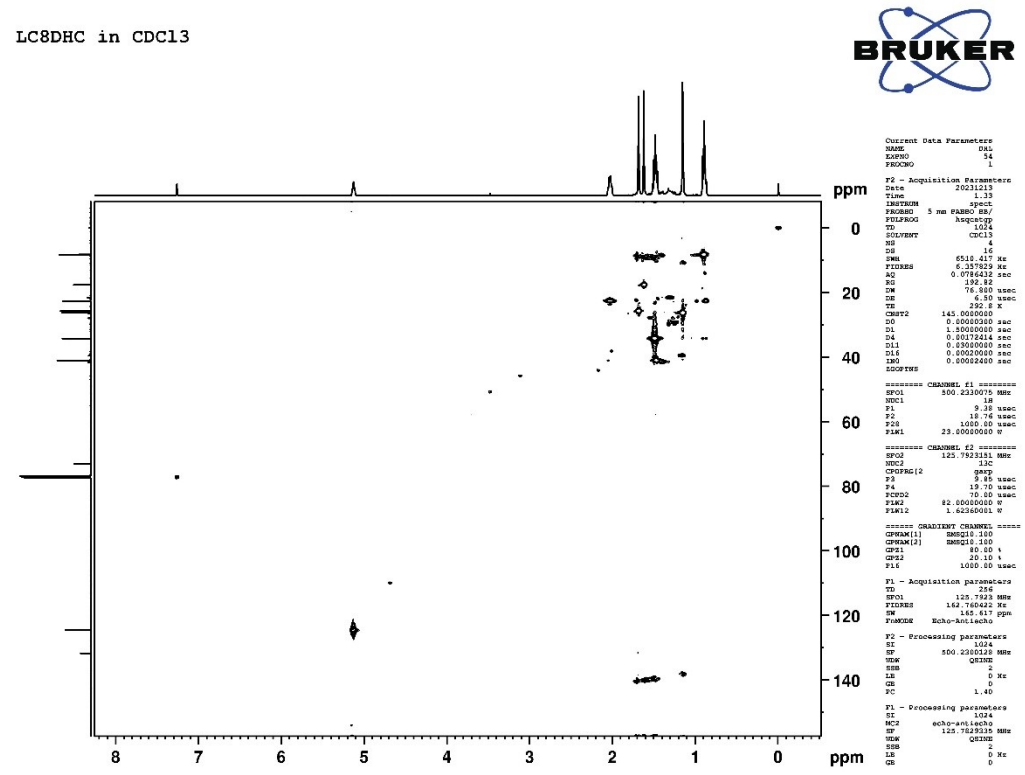

Figure S12.7 ^{1}H-^{13}C HSQC spectrum of reaction product (II)

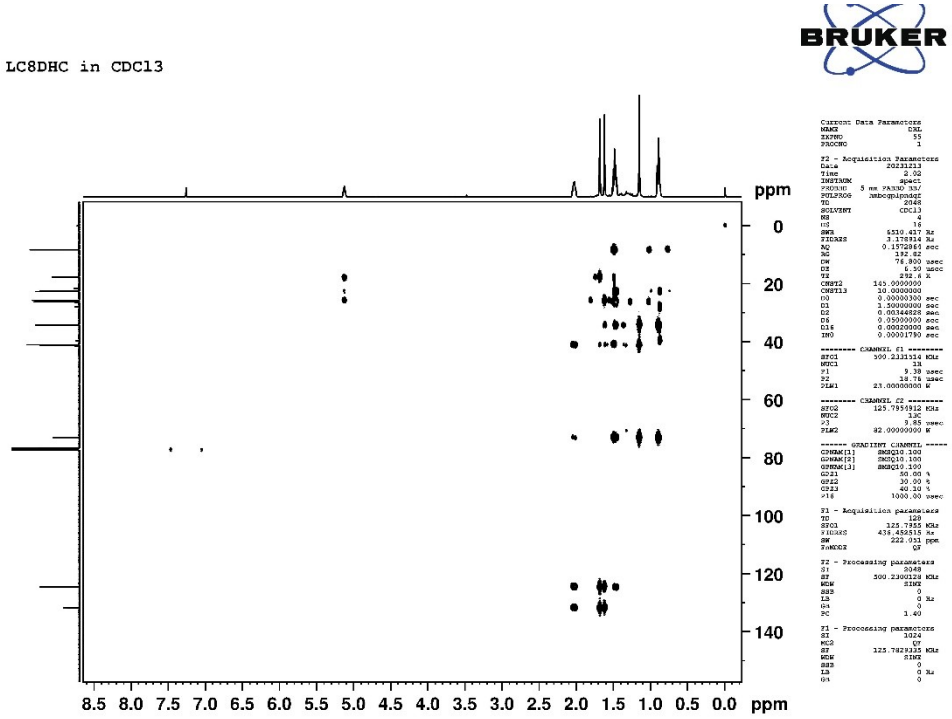

Figure S12.8 ^{1}H-^{13}C HMBC spectrum of reaction product (II)

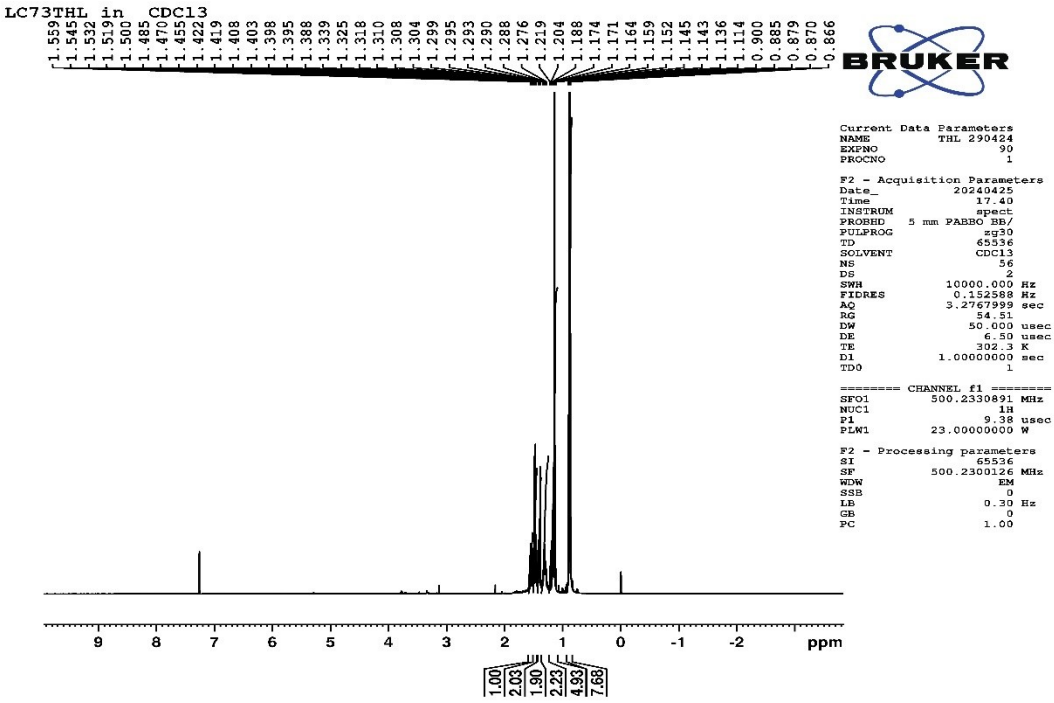

Figure S13.1 1H-NMR spectrum of reaction product (III)

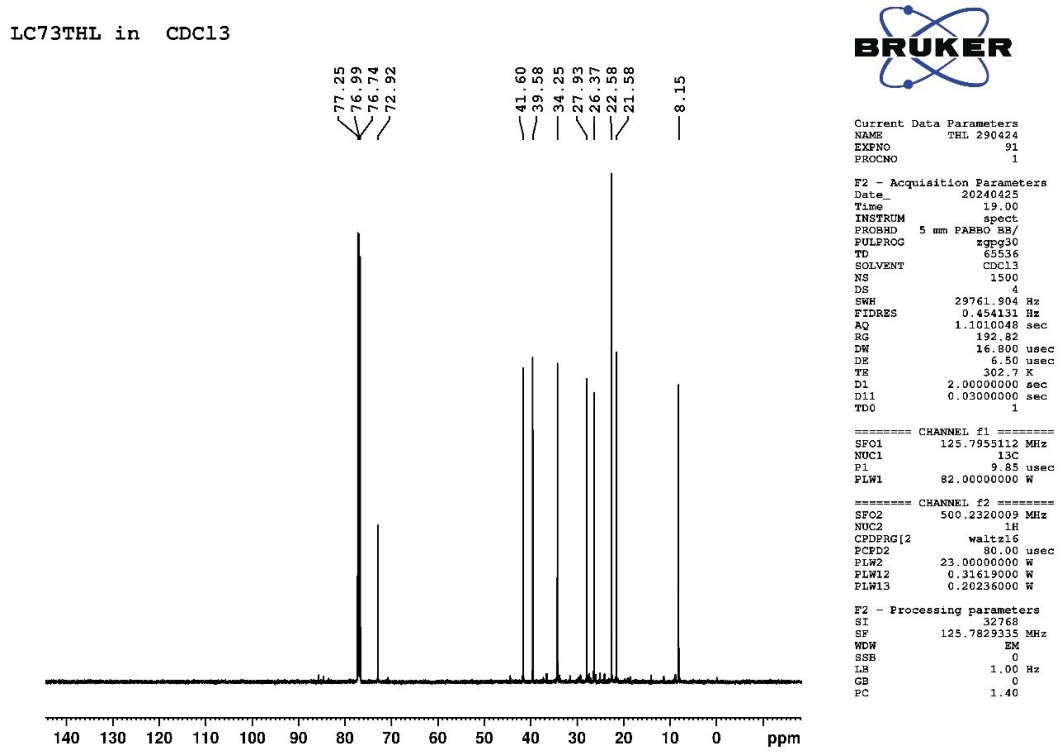

Figure S13.2 ^{13}C-NMR spectrum of reaction product (III)

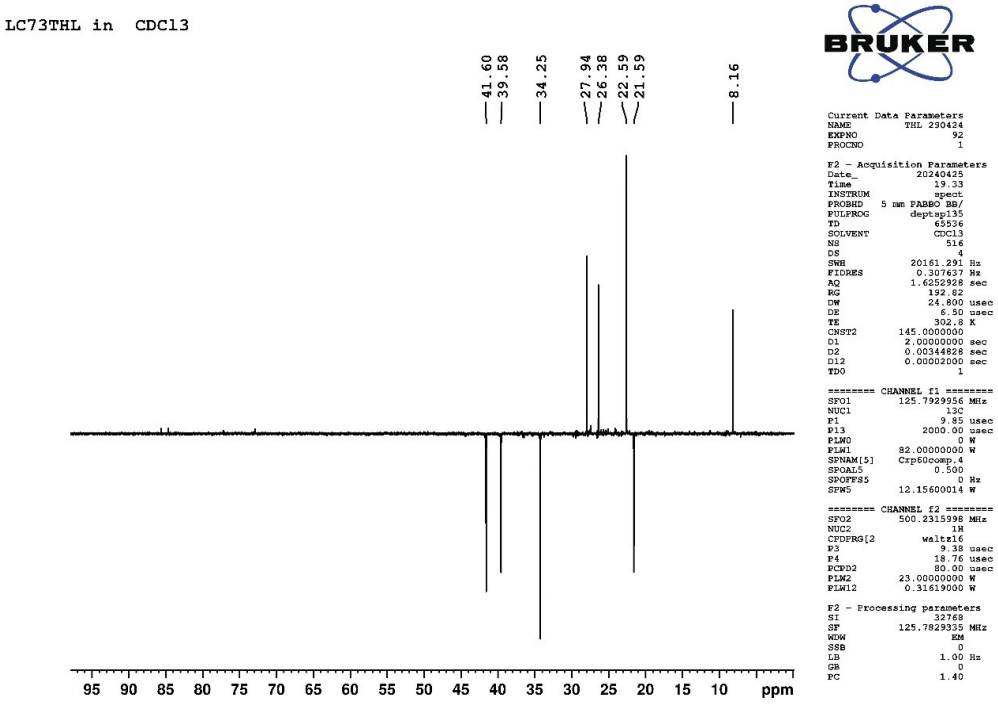

Figure S13.3 DEPT-135° spectrum of reaction product (III)

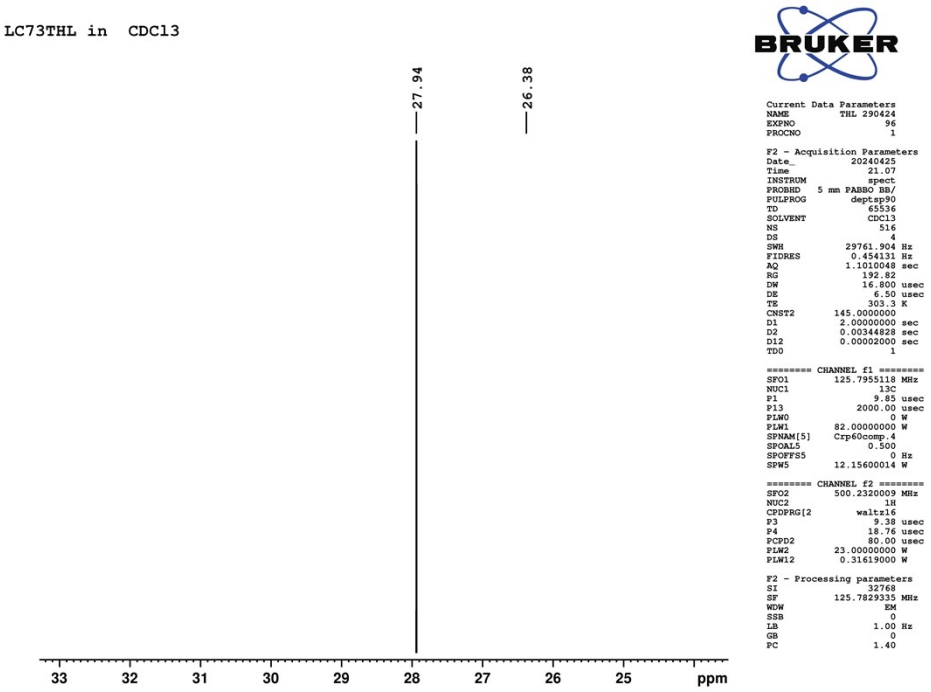

Figure S13.4 DEPT-90°spectrum of reaction product (III)

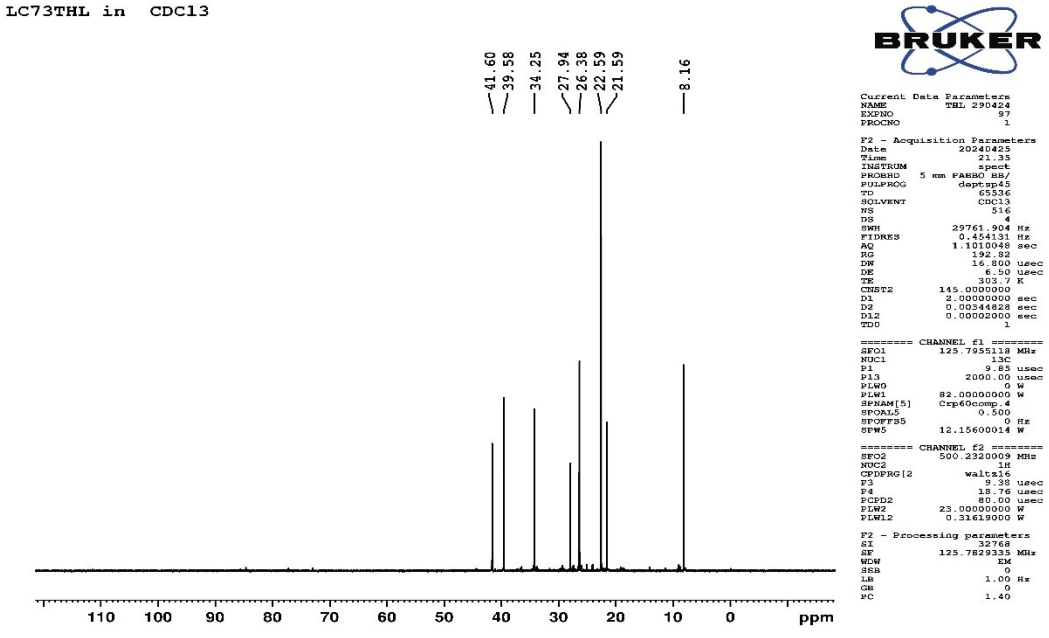

Figure S13.5 DEPT-45°spectrum of reaction product (III)

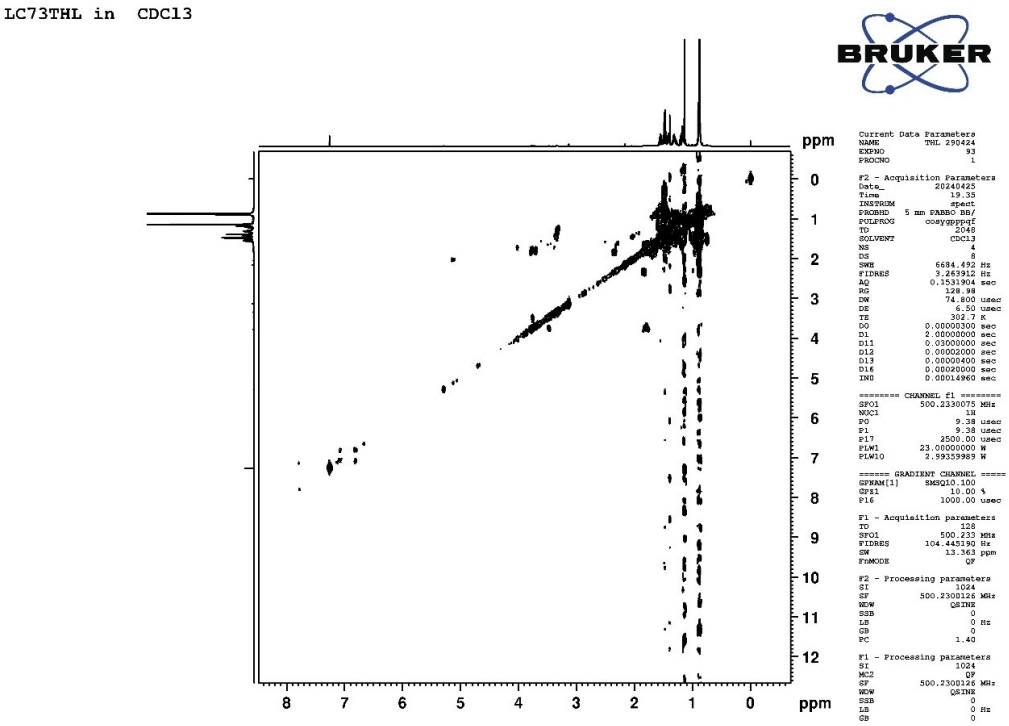

Figure S13.6 ^{1}H-^{1}H COSY spectrum of reaction product (III)

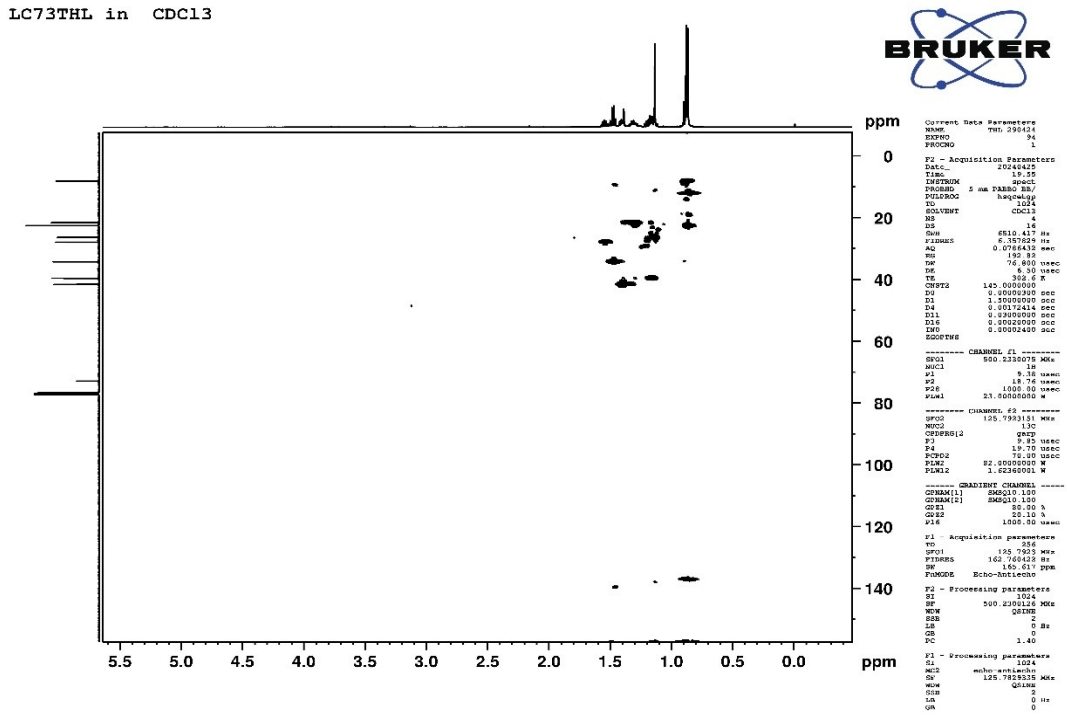

Figure S13.7 ^{1}H-^{13}C HSQC spectrum of reaction product (III)

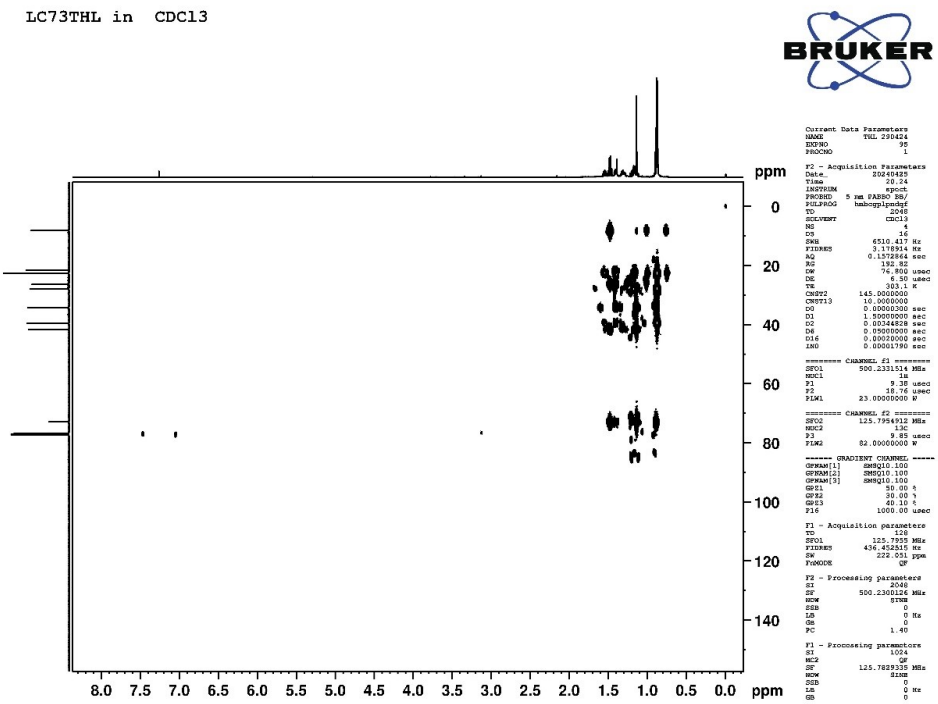

Figure S13.8 ^{1}H-^{13}C HMBC spectrum of reaction product (III)

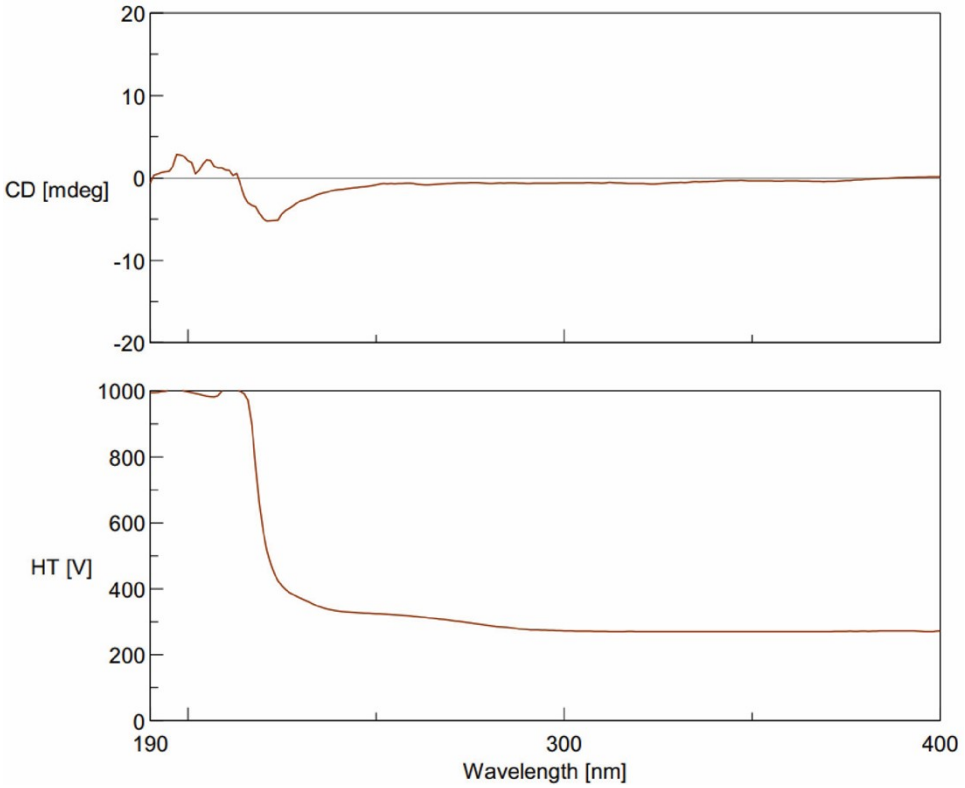

Figure S14.1 CD spectra of reaction substrate (I)

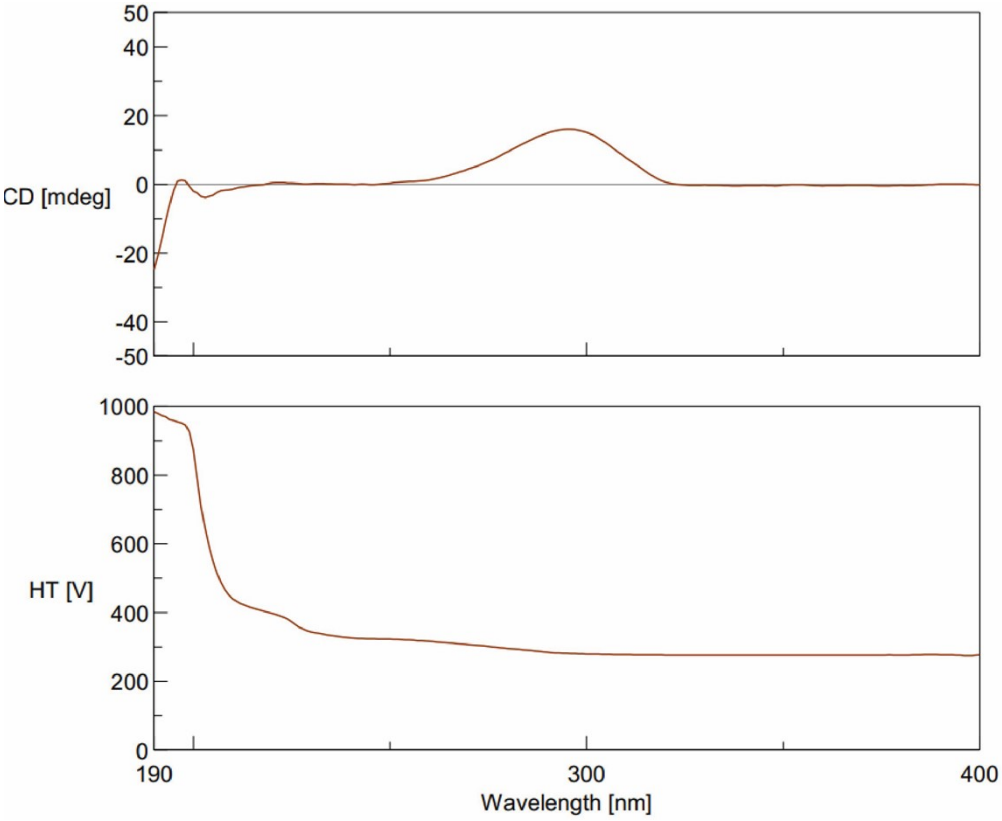

Figure S14.2 CD spectra of reaction product (III)

References

[1] J.F. Clevenger, Apparatus for the Determination of Volatile Oil*, J. Am. Pharm. Assoc. 17 (1928) 345–349. https://doi.org/10.1002/jps.3080170407.

[2] P. Kumar, P.K. Sharma, S. Chaturvedi, C.S. Chanotiya, P.R. Rauta, P. Mohapatra, P.K. Rout, Synthesis of Ni-Doped Hydrotalcite Catalyst Through Hydrothermal Process for the Selective Reduction of α,β-Unsaturated Aldehyde (Citral) to Enantiospecific (+)-Citronellal, Catal. Letters 153 (2023) 3019–3030. https://doi.org/10.1007/s10562-022-04195-w.

[3] B. Qi, L. Di, W. Xu, X. Zhang, Dry plasma reduction to prepare a high performance Pd/C catalyst at atmospheric pressure for CO oxidation, J. Mater. Chem. A 2 (2014) 11885. https://doi.org/10.1039/C4TA02155J.

[4] M. Mansor, S.N. Timmiati, W.Y. Wong, A. Mohd Zainoodin, K.L. Lim, S.K. Kamarudin, NiPd Supported on Mesostructured Silica Nanoparticle as Efficient Anode Electrocatalyst for Methanol Electrooxidation in Alkaline Media, Catalysts 10 (2020) 1235. https://doi.org/10.3390/catal10111235.

[5] Y. Zhang, Y. Liao, G. Shi, W. Wang, B. Su, Preparation, characterization, and catalytic performance of Pd-Ni/AC bimetallic nano-catalysts, Green Process. Synth. 9 (2020) 760–769. https://doi.org/10.1515/gps-2020-0071.

[6] H. Štorkánová, S. Oreská, M. Špiritović, B. Heřmánková, K. Bubová, M. Komarc, K. Pavelka, J. Vencovský, J.H.W. Distler, L. Šenolt, R. Bečvář, M. Tomčík, Plasma Hsp90 levels in patients with systemic sclerosis and relation to lung and skin involvement: a cross-sectional and longitudinal study, Sci. Rep. 11 (2021) 1. https://doi.org/10.1038/s41598-020-79139-8.

[7] K. Park, K.R. Lee, S. Ahn, H. Park, S. Moon, S. Yoon, K.-D. Jung, Investigating the Catalytic Deactivation of a Pd Catalyst during the Continuous Hydrogenation of CO2 into Formate Using a Trickle-Bed Reactor, Catalysts 14 (2024) 187. https://doi.org/10.3390/catal14030187.

[8] Z. Sun, Y. Han, M. Gao, X. Wei, X. Hu, Cetyl Trimethyl Ammonium Bromide-Assisted Electrochemical Preparation of Palladium-Nickel Bimetallic Electrode, Int. J. Electrochem. Sci. 6 (2011) 5626–5638. https://doi.org/10.1016/S1452-3981(23)18433-1.

[9] S. Singha, M. Sahoo, K.M. Parida, Highly active Pd nanoparticles dispersed on amine functionalized layered double hydroxide for Suzuki coupling reaction, Dalt. Trans. 40 (2011) 7130. https://doi.org/10.1039/c1dt10697j.

[10] N. Pal, Nanoporous metal oxide composite materials: A journey from the past, present to future, Adv. Colloid Interface Sci. 280 (2020) 102156. https://doi.org/10.1016/j.cis.2020.102156.

[11] M.. Donohue, G.. Aranovich, Classification of Gibbs adsorption isotherms, Adv. Colloid Interface Sci. 76–77 (1998) 137–152. https://doi.org/10.1016/S0001-8686(98)00044-X.

[12] E.M. Mistar, T. Alfatah, M.D. Supardan, Synthesis and characterization of activated carbon from Bambusa vulgaris striata using two-step KOH activation, J. Mater. Res. Technol. 9 (2020) 6278–6286. https://doi.org/10.1016/j.jmrt.2020.03.041.

[13] R.P. Adams. Identification of Essential Oil of Components by Gas Chromatography/Mass Spectrometry, Ed. 4.1. USA. Allured Publishing Corporation, Carol Stream, Illinois (2017)

[14] C.S. Chanotiya, Y. Pant, R.K. Lal, P. Kumar, P. Kumar, L. Bawitlung, M. Semwal, P.K. Trivedi, A. Pal, Radiocarbon (14C) accelerator mass spectrometry as a convenient tool for differentiation of flavor chemicals of synthetic origin from biobased sources and their in-vivo toxicity assessment, Sci. Total Environ. 908 (2024) 168357.

https://doi.org/10.1016/j.scitotenv.2023.168357.